



Design and characterization of a source of ultrashort electron pulses at a MHz repetition rate

Diplomarbeit

von

Daniel Wytrykus

*angefertigt am Lehrstuhl für Experimentalphysik – Quantenoptik
von Prof. Dr. Ferenc Krausz
Ludwig-Maximilians-Universität München*

*betreut durch Prof. Dr. Alfred Laubereau
Lehrstuhl für Quantenoptik und ultraschnelle Phänomene
Physik-Department der Technischen Universität München*

5.2.2008

Contents

1	Introduction	1
2	Concepts	5
2.1	Time-resolved electron diffractometry	5
2.2	Limits of time resolution in UED experiments	7
2.3	The way towards ultrashort electron pulses	9
2.3.1	The energy spread induced in the RF cavity	11
2.3.2	Synchronization of RF field with pulse timing	15
2.4	The role of the photoelectron energy distribution	18
3	Computer simulations	21
3.1	The simulation system	21
3.2	Modeling the setup	22
3.3	Selected simulation results	24
3.3.1	Evolution of electron pulse length	24
3.3.2	Space-charge	27
3.3.3	Electric field inhomogeneities at the anode	28
3.3.4	Timing errors of the AC field with respect to electron arrival . .	30
4	Experimental work	31
4.1	Experimental setup and methods	31
4.1.1	The laser system	31
4.1.2	Higher-harmonic-generation from the laser output	37

4.1.3	The electron gun	44
4.2	Results and discussion	49
4.2.1	Electron yield from the cathode	49
4.2.2	Electron beam profile	55
4.2.3	Initial electron energy distribution	58
5	Conclusion	67
	Appendix	69
	Bibliography	73
	Acknowledgement	77

Chapter 1

Introduction

In the course of the 20th century, the science of physics penetrated deeper and deeper into the previously unknown world of the smallest structures and fastest processes — the world of quantum mechanics. A huge variety of new experimental methods to address those incredibly small scales had to and has been developed, pushing the frontiers of spatial and temporal resolution further and further. With the advent of pulsed laser technology, a new means of investigating extremely fast processes became available: laser pulses with durations in the regime of femtoseconds ($1 \text{ fs} = 0.000\ 000\ 000\ 001 \text{ s}$), so-called ultrashort pulses, provided access to processes far beyond the temporal resolution limits of even the fastest possible electronics. A new field of research evolved: time-resolved spectroscopy, mainly based on the pump-probe-technique, which means that a high-energy laser pulse excites a specimen and another (weak) laser pulse arrives at the specimen with some defined time delay with respect to the first pulse, hence “reading out” the state of the specimen *at* the chosen time after its excitation. Thus, it is possible not only to examine stationary states of atoms and molecules, but to look into the details of what happens between an excitation and the system’s return to equilibrium, what transient states occur. Only some years ago, even the attosecond regime ($1 \text{ as} = 0.001 \text{ fs}$) came into reach for experiments in the time domain, with few-cycle pulses of extreme ultraviolet light [1].

However, no matter how high the time resolution of laser spectroscopy gets, there are fundamental limits concerning the spatial resolution — in this respect, laser experiments with visible or even ultraviolet light are restricted to the light wavelength in the range of tens to hundreds of nanometers. Thus, they cannot resolve small molecular or atomic structures, where typical dimensions are in the Ångström and sub-Ångström regime ($1 \text{ Å} = 10^{-10} \text{ m}$). Within certain limits, structural changes in the specimen can be inferred from the observed spectroscopic behavior, but this is a quite indirect way to get spatial information and it is necessarily based on many assumptions about the structure, because a measurement in one dimension (time) cannot reveal the full information about three other dimensions (space).

Now the key question arises, how to address directly the ultrafast dynamics of atomic and molecular structures. Of course, in principle it is possible to generate very short X-ray bursts, but facilities that produce X-ray pulses which are both short and intense enough are large and expensive. So the idea came up to produce ultrashort pulses

of charged particles, particularly electrons. Their main advantage is their very small effective (de Broglie-) wavelength:

$$\lambda = \frac{h}{p} \quad (1.1)$$

According to Einstein's relativistic energy formula

$$E^2 = (pc)^2 + (mc^2)^2 \quad (1.2)$$

the momentum p is given by

$$p = \frac{1}{c} \sqrt{E^2 - (mc^2)^2} \quad (1.3)$$

One obtains, e.g. for an electron (rest energy 511 keV) with 20 keV kinetic energy ($E = 531$ keV):

$$\lambda = 8.6 \cdot 10^{-12} \text{ m} \approx 0.1 \text{ \AA}$$

Hence, an electron beam in the keV energy range, which is easily realizable in the laboratory, can provide a high enough spatial resolution in the sub-Å regime. This fact can be exploited by observing the diffraction of the beam by a target (specimen) and using the well-established methods of diffraction analysis [2].

In addition, electron beams have other advantages. In contrast to X-ray photons, electrons are scattered by both the atomic nucleus and the atom's electron distribution around the nucleus (via Coulomb scattering), and the cross-section for electron Coulomb scattering is about six orders of magnitude higher than for the Thomson scattering of X-rays. Consequently, much lower particle fluxes are required. At the same time, if one considers inelastic scattering (which is usually an undesired side effect), the energy deposited in the specimen *per* inelastic scattering event is much lower for electrons than for X-rays [3], and as the number of inelastic scattering events is proportional to the particle flux, several orders of magnitude less energy is deposited in the specimen by inelastic scattering in the case of electron scattering.

Electron diffraction with high time resolution down to about 1 ps is already established as a tool to study fast dynamics in molecules in gas phase or crystal surface dynamics. It is called UED (ultrafast electron diffraction), and very important contributions to this field of research came from Ahmed H. Zewail and his group [3, 4].

A pulsed electron beam, i.e. a train of equidistant short electron pulses, is produced by sending ultrashort laser pulses onto a cathode, where electrons are excited into the vacuum via the photoelectric effect during the short duration of each laser pulse, and those free electrons are immediately accelerated in a static electric field between the cathode and an anode. Behind the anode, the pulsed electron beam can be directed and focused onto a sample, and an electron detector with high spatial resolution can collect data about the spatial (angular) distribution of the electrons after the diffraction

process (i.e. the diffraction image of the sample). The fact that the electron pulses are generated by laser pulses is the key point: It means that one can rely on the highly advanced ultrashort laser pulse technology and exploit the well proven precision of the pump-probe technique. In contrast to spectroscopy, a probe pulse in the form of an electron bunch is not sensitive to optical resonances, but to the spatial structure of the sample at the chosen moment after excitation with sub-atomic resolution.

In pump-probe experiments, the time resolution is mainly defined by the duration of both the pump and the probe pulse (see chapter 2). For laser light, it is already state of the art to produce pulses which are as short as a few femtoseconds — however, the time resolution in UED has been limited till today by the electron pulse duration on reaching the specimen, which never went far below 1 ps, even though their initial duration (in the moment of photoemission) is clearly limited by the femtosecond laser pulse duration. This is, for the most part, due to the following two reasons:

- Electron bunches from photoemission possess an energy spread which leads to a rapid pulse broadening during acceleration, as some particles in the bunch travel faster than other particles.
- All electrons in a bunch repel each other by Coulomb interaction, enhancing the pulse broadening process (space-charge effect).

Both mechanisms act so severely on electron bunches that the pulse duration increases drastically even for very short propagation times, which cannot be reduced arbitrarily for technical and practical reasons. One cannot avoid the particles' path through an acceleration stage, and in many cases it is necessary to manipulate the particle beam (e.g. to focus it) before it reaches the sample, which again implies additional path length.

This thesis is part of a project at the Ludwig-Maximilians-Universität München, where a new table-top electron pulse source is developed which shall, for the first time, provide electron pulses in the energy range of 10 – 40 keV which are as short as a few femtoseconds. With this electron gun, UED experiments with unprecedented spatial and temporal resolution will become possible. The basic idea of how to achieve such ultrashort pulse durations consists of the following two steps:

1. The number of electrons per pulse is reduced to a few (on the order of one electron), rendering the space charge broadening ineffective. At the same time, the pulse repetition rate is increased by orders of magnitude, to keep the average particle flux comparable to existing UED systems and to keep the integration times at the detector low.
2. The electrostatic acceleration is complemented by a time-dependent electric field, in the form of a standing electromagnetic wave inside a radio frequency (RF) cavity, which can compensate for the energy spread in the electron bunch and actively “focuses” the particles in time onto the target (active pulse compression, or “bunching”).

The first step implies that there is a laser available which delivers ultrashort pulses with sufficient energy and a high enough (MHz) repetition rate. Such a laser has been developed during the last years [5] and was available for this project.

The second step is based on well known and widely applied particle accelerator technology, but the big technical challenge here is to synchronize the AC field and the electron pulses with very high precision [6]. Furthermore, the application of an RF cavity for such a tight temporal focusing of electron bunches has, to my knowledge, not been realized yet. However, theoretical studies confirm the possibility to compress electron bunches even to sub-femtosecond durations with appropriate time-dependent fields [6, 7, 8].

In the frame of this thesis, the first of the steps outlined above was made, which means a new electron gun was built and then driven with femtosecond oscillator pulses at MHz repetition rate — with the laser fundamental as well as its second and third harmonic, to optimize the electrons' energy spread due to photoemission. The scenarios were compared, and the electron gun was characterized. Furthermore, simulations were carried out with the setup's parameters to compare theoretically expected behavior with the observed behavior, and to estimate how effective electron pulse compression will work in the future setup with the RF cavity.

Chapter 2

Concepts

2.1 Time-resolved electron diffractometry

As already stated in the introduction, the small wavelength of electrons at energies of several thousand keV allows to resolve structures on the molecular and atomic scale by diffraction: the particle beam passes through a specimen, the electrons' matter waves are diffracted, and behind the specimen the beam forms a diffraction pattern which contains information about the structure of the sample on a scale of the particles' wavelength (see fig. 2.1). By exploiting this principle, even the probing of the time evolution of structures is possible, as was treated extensively in [9]. The feasibility of time-resolved electron diffraction has been demonstrated and already been used to gain insight into ultrafast dynamics [3, 4, 10, 11]. The trick which enables physicists to achieve a time resolution which is far out of reach of any electronics is the pump-probe technique; see fig. 2.2 for a schematic description. In UED, the probe beam is a pulsed electron beam which is triggered by laser pulses at the cathode of the electron gun. So the scheme works in the same way as for ultrafast laser spectroscopy, the only difference being that one has to take into account the slower propagation of the electrons in order to get the proper delay at the target.

What all modern experiments have in common besides the usage of the pump-probe principle, is the elementary UED apparatus design, see fig. 2.3. Usually the cathode is a disc of optically transparent material, with the actual cathode material (in most cases, copper or a noble metal) deposited on one side of the disc as a thin film of a few tens of nanometers. The films are so thin in order to allow the light to penetrate the whole metal layer and therefore to release photoelectrons from its surface (metal–vacuum interface). The anode is typically just a grounded flat metal surface with a small aperture to allow the electron beam to pass through, or it is a very fine-meshed metal grid (like those used in electron microscopy) with the aperture behind the grid. If the sample under investigation is a gas, the target takes the form of a gas jet emitted from a nozzle into the vacuum of the target chamber; in this case, differential pumping is used to enable a high enough vacuum in the acceleration chamber in spite of the gas in the target chamber. As a one-dimensional or better two-dimensional spatial resolution is needed for diffraction image acquisition, the detector is usually a CCD

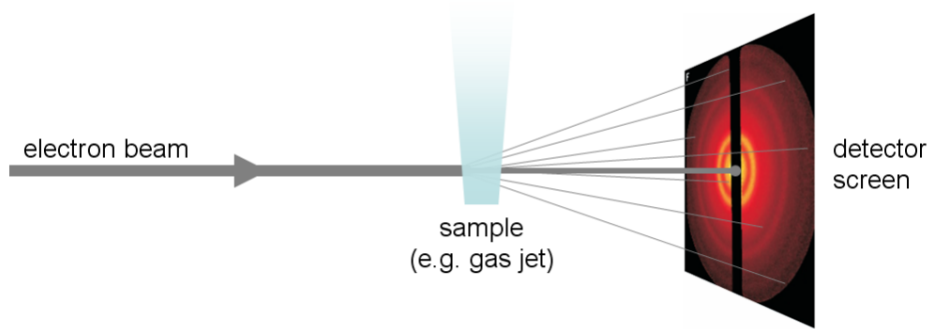


Figure 2.1: Principle of an electron diffraction experiment: The particle beam passes through the sample, in this case a gas jet where the electrons encounter all possible orientations of the gas molecules — depending on the spatial structure of the molecules, certain amounts of momentum transfer during the elastic scattering are especially probable. The electrons experiencing these momentum transfers spread out in cones from the sample, which appear on the detector screen in the form of rings.

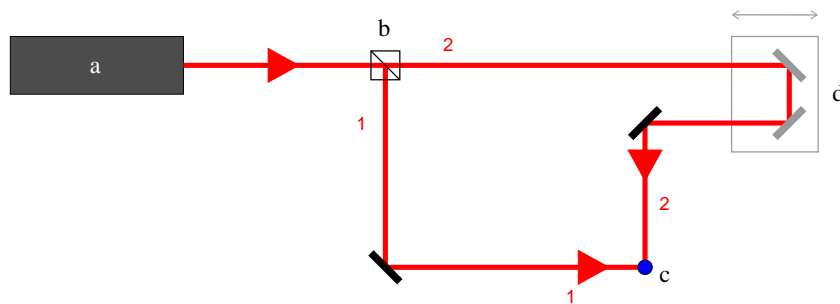


Figure 2.2: The pump-probe technique: laser source (a) produces ultrashort laser pulses which are split up in two beam arms by an optical splitter (b), where beam 1 serves as the pump beam and beam 2 as the probe beam. If both beam arms had the same optical path length, the pulses in both arms would arrive at target (c) at exactly the same time. By increasing the path length for beam 2 via a so-called delay line (d), the probe pulse can be delayed with respect to the pump pulse by an amount of time which can be controlled very precisely by the variable delay line length.

(charge-coupled device) camera from which the image can be read out and processed digitally. In some cases the electrons hit the CCD directly (direct bombardment) and generate the necessary electronic signal by their impact, but usually a scintillating screen is installed in front of the CCD, producing a number of photons for every electron (depending on its energy), and this light is coupled to the CCD via a fiber optic taper or a lens system. To acquire a single diffraction image, integration times on the order of minutes are necessary.

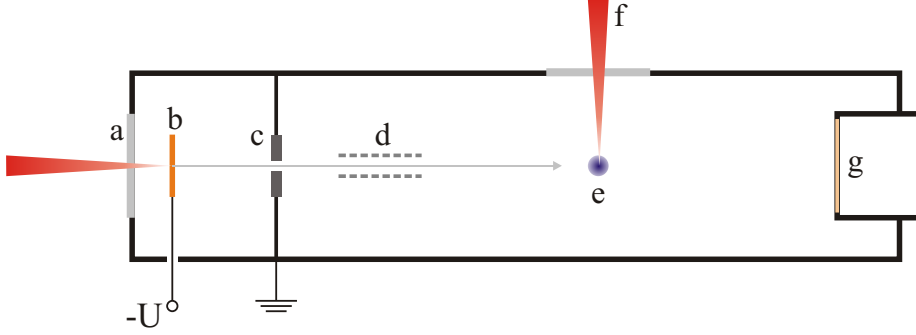


Figure 2.3: Typical scheme of a UED experiment: laser beam from the probe arm enters high-vacuum chamber through a window (a), being focused onto the photocathode (b) which is kept at a highly negative electrostatic potential $-U$, so that the emitted photoelectrons are accelerated towards the anode (c), which is grounded. The electron beam might be steered and/or focused by electron optics (d) before reaching the target (e). A pump laser pulse (f) initiates dynamics in the specimen before the electrons arrive and get diffracted. Transmitted electron beam as well as diffracted electrons are incident on a detecting screen (g).

2.2 Limits of time resolution in UED experiments

Obviously, the time resolution of a pump-probe experiment is defined by the duration of interaction of the “detecting pulse” (probe pulse) with the system under investigation, which is the duration of the probe pulse itself (in case of UED, the electron pulse). In practice, there are some additional effects playing a role for the time resolution. For pump-probe experiments, and UED in particular, the following factors pose limits to the achievable time resolution:

- length of the probe (electron) pulse τ_e
- length of the pump pulse τ_p initiating the dynamics in the sample
- velocity mismatch between electrons and light ($\rightarrow \Delta t_{VM}$)

Assuming Gaussian time profiles for the pulses, the total time resolution τ for the pump-probe experiment can be expected to be ([3], p.1781)

$$\tau = \sqrt{\tau_e^2 + \tau_p^2 + \Delta t_{VM}^2} \quad (2.1)$$

The following is a short discussion of the above-named contributions:

The most critical point, which is primarily addressed in this thesis and the future project, is of course the electron pulse duration. This point is therefore discussed in detail in section 2.3.

The laser pulse length is a parameter which can be controlled quite precisely in modern lasers, and in principle very short pulse durations on the order of femtoseconds can

be achieved. However, the laser system which is used for this project does currently not allow for pulses much shorter than about 70 fs, due to its very special design which was chosen to get the necessary MHz repetition rate; see chapter 4.1 for details. But for all existing UED setups, even this relatively long pulse duration would have much less impact on the total time resolution than the electron pulse length, which is usually about 1 ps, and the velocity mismatch (see below) can easily make up a larger contribution as well.

This third contribution is connected to the different speeds of light and electron pulses and the finite spatial latitude of the target (interaction volume), which is, e.g. for a gas-phase UED experiment, given by the diameter of the gas jet of target molecules, d_M . To simplify matters, consider collinear pump (laser) and probe (electron) beams. The light pulse travels faster than the electron bunch by a factor $\kappa = c/v_e$. When the two pulses enter the target volume, they have a certain relative time delay with respect to each other. When they leave the volume, after the transit through the interaction volume, this delay has changed due to the different amounts of time the pulses needed to traverse the volume (to cover the distance d_M):

$$\Delta t_{VM} = \frac{d_M}{v_e} - \frac{d_M}{c} = \frac{d_M}{c}(\kappa - 1) \quad (2.2)$$

For $\kappa \rightarrow 1$, i.e. ultrarelativistic electrons, the effect of the velocity mismatch vanishes. But for electrons with 20 keV of kinetic energy, $\beta = 0.27$, which implies $\kappa = 1/\beta = 3.7$.

In [12], the issue is discussed in more detail, and a formula for the more general case of arbitrary intersection angles between laser and electron beam is derived. In particular, an optimum angle θ_{min} is found for which the effect of the velocity mismatch is minimal, *if* the spatial laser pulse width d_L is smaller than $d_M\sqrt{\kappa - 1}$, which should usually be the case:

$$\Delta t_{VM}(\theta_{min}) = \frac{d_L}{c} \sqrt{\frac{(\kappa^2 - 1) - d_L^2/d_M^2}{1 + d_L^2/d_M^2}} \quad (2.3)$$

E.g. for a laser beam diameter $d_L = 100 \mu\text{m}$ and a gas jet diameter $d_M = 200 \mu\text{m}$, one obtains for 20 keV electron pulses

$$\Delta t_{VM}(\theta_{min}) = 1.1 \text{ ps}$$

This value gives the impression that femtosecond UED is not possible in a setup described above, but the problem of pulse velocity mismatch can be overcome by spatially tilting the laser pulses, as was demonstrated in [13].

2.3 The way towards ultrashort electron pulses

There are several different suggestions how to approach the femtosecond and attosecond regimes in electron pulse duration:

- generation of attosecond electron bunches at the boundary of an overdense plasma with extremely high laser intensity [14]
- slicing ultrashort electron pulses out of long bunches via ponderomotive force of either laser pulses [13] or surface plasmons [15]
- production of relativistic electron bunches (with MeV energies) to minimize space-charge broadening [16]
- generation of single-electron pulses to avoid space-charge broadening [6, 17, 19]
- active temporal electron pulse compression using a temporal lens [18, 6, 19]

The first two ideas have, to my knowledge, not yet been realized experimentally. The third possibility was investigated with the aim of reaching 100 fs resolution in single-shot diffraction experiments (i.e. huge numbers of electrons per bunch) and requires the expensive infrastructure of a high-energy electron accelerator.

The project in which this thesis is embedded concentrates on the combination of the latter two suggestions. On the one hand, the number of electrons per pulse shall be kept around one while the pulse repetition rate is high enough to keep up a viable electron flux. In most modern UED experiments, the electron gun is driven by strongly amplified laser systems with kHz repetition rate and pulse energies up to the mJ regime. In our case, a special laser system with MHz repetition rate and pulse energies close to the μJ regime is used, so the average photon rate (or laser power) is about the same, and with it, the electron rate (since very similar photocathodes are used).

On the other hand, the electron pulses shall be focused in time with a temporal lens in the form of a radiofrequency (RF) cavity directly behind the static acceleration stage. Inside this cavity, a standing electromagnetic wave is maintained, which constitutes nothing else than a time-dependent acceleration field for the electrons that induces a chirp¹ on the pulse, leading to self-compression of the pulse during further propagation (see fig. 2.4). This “bunching” principle is widely used in large-scale particle accelerators.

Talking about single-electron pulses, it is worth mentioning that the *pulse duration* is of course not defined for a single pulse, but has to be understood rather as a statistical value, indicating how far the arrival times of those single particles deviate statistically from an optimum arrival time at a given point in space. In the frame of this thesis, the electron pulse duration is defined as the standard deviation of such an arrival time distribution. An adapted concept of a temporal *pulse shape* (analogous to the squared

¹The term “chirp” is used here in full analogy to its meaning in laser pulse physics: it is a time-dependent deviation of the particles’ energy from the bunch’s center energy, where time dependence is to be understood as the longitudinal and therefore temporal location of the particle in the bunch

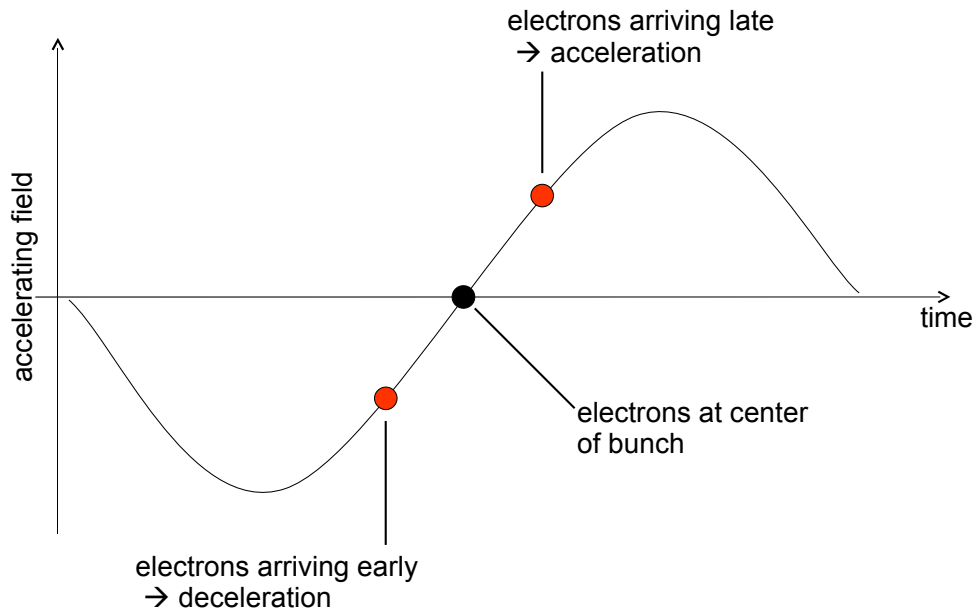


Figure 2.4: Bunching: temporal compression of electron pulses by means of an oscillating electric field. Pulses and field oscillation must be synchronized in order to make the pulse center arrive at the moment of zero-crossing of the field.

pulse envelope in laser physics) can be found accordingly: It can be defined as the shape of the distribution in time that is given by a histogram of the number of particles (from a large number of pulses) versus their arrival time relative to the optimum (or center) arrival time, as illustrated in fig. 2.5.

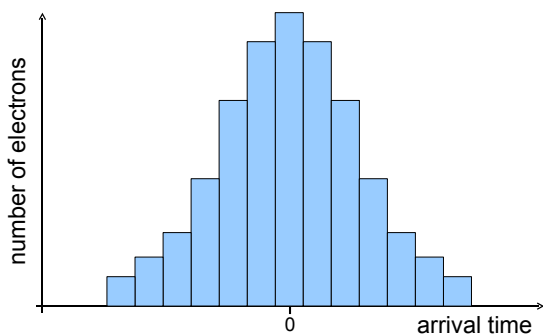


Figure 2.5: Effective pulse shape of single-electron pulses as a histogram of arrival times at a given location in space. (This shape is just an example; in general it is not symmetric.)

If space-charge does not play a role (as in our case), there are two reasons why the electrons do not always arrive at the target at the same time (which would be equivalent to a zero pulse duration):

- different starting times
→ temporal aberration
- different energies or velocities
→ chromatic aberration

The first point means that there is already a finite electron pulse length at the moment of photoemission, before the acceleration plays a role, depending on the finite laser pulse duration. The second one means that there are differences in the kinetic energies which the electrons possess right after the photoemission process (see section 2.4 for details) — this leads to a spreading of the pulse due to different velocities.

It can be shown theoretically that, to first order, both effects can be made zero simultaneously through bunching with appropriate time-dependent fields [7, 8]. In this regard, temporal focusing behaves similar to spatial focusing. So if the first-order contribution to the pulse length is zero, the pulse length is defined by higher-order contributions, and one can get to the following relation (see [18], eq. 14):

$$\tau_f \varepsilon_f \approx 2\tau_i \varepsilon_i \quad (2.4)$$

where τ_f , ε_f are electron pulse duration and energy spread at the point of temporal focus (the target point), and τ_i , ε_i the initial pulse duration and energy spread directly after photoemission. It is obvious from this relation that the minimum pulse duration (in the temporal focus) can even be much smaller than the initial one, if the energy spread is increased accordingly. Assuming an ideal bunching, the laser pulse duration does not limit the achievable electron pulse duration, as long as the AC field induces enough energy spread on the bunch.

To check the feasibility of the proposed scheme, one has to consider particularly the following two critical points:

- How much energy spread must the AC field induce and is this possible with a manageable intracavity RF power?
- Is it possible to synchronize the AC field with the pulse timing with high enough precision?

Note that, as far as no other references are given, most of the following discussion is based on [19].

2.3.1 The energy spread induced in the RF cavity

The induced energy spread is dependent on the time difference between electrons in the pulse front and the tail, as they arrive at the temporal lens, the RF cavity. The considered setup is depicted in fig. 2.6.

The larger contribution to the arrival time difference at the cavity results from the initial energy spread — it can be estimated as follows. Let the DC acceleration voltage be $U = 20$ kV, and for 20 keV electrons we have $\beta = 0.27$ and $\gamma = 1.04$, so for a rough estimation it is enough to use the nonrelativistic equation of motion for electrons in the accelerating field:

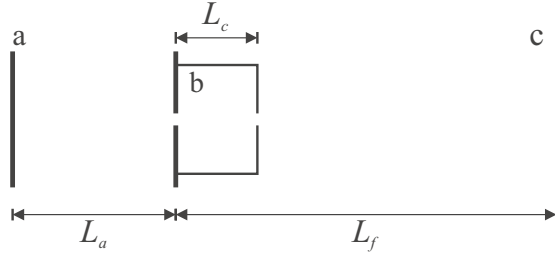


Figure 2.6: Basic scheme of the electron gun with RF cavity, with dimensions used in the formulas below. (a) cathode, (b) anode and cavity, (c) plane of temporal focus. The electrons enter and exit the cavity through small holes in its front and back wall.

$$F = ma = e \frac{U}{L_a} \quad (2.5)$$

where m is the electron mass and L_a is the distance from cathode to anode. So the acceleration is

$$a = \frac{eU}{mL_a} \quad (2.6)$$

and every electron gains the kinetic energy $E = eU$ while it travels through the potential difference U in the DC acceleration stage. From $a = dv/dt$ we get the arrival time difference due to energy or velocity spread (chromatic aberration):

$$\Delta t_{chrom} = \frac{1}{a} \Delta v \quad (2.7)$$

The velocity difference Δv between electrons with zero initial energy and with highest initial energy (equal to the initial energy spread ε_i) stays constant throughout the acceleration process and is given by

$$\Delta v = \Delta v_i = \sqrt{\frac{2\varepsilon_i}{m}} \quad (2.8)$$

Combining the above equations, one obtains

$$\Delta t_{chrom} = \frac{L_a}{eU} \sqrt{2m\varepsilon_i} = \frac{\sqrt{2m\varepsilon_i}}{e\mathcal{E}} \quad (2.9)$$

where \mathcal{E} is the static electric field. For DC acceleration, the chromatic aberration in arrival time is proportional to the square root of the energy spread, with the proportionality constant $\sqrt{2m}/e\mathcal{E}$, which is also known as the Zavoisky-Fanchenko constant [18] (sometimes different powers of the elementary charge e occur due to different systems of units).

Assuming that initial electron energies and their emission times are not correlated, the full difference in arrival times Δt (i.e. the electron pulse length τ) at the cavity is given by the combination of chromatic and temporal aberration, where the latter is simply the initial pulse length τ_i :

$$\tau = \Delta t = \sqrt{\Delta t_{chrom}^2 + \Delta t_{temp}^2} = \sqrt{\Delta t_{chrom}^2 + \tau_i^2} \quad (2.10)$$

To make the “advanced” electrons (in the pulse front) arrive at the target (distance L_f) simultaneously with the delayed electrons (in the pulse tail), the AC field in the cavity has to redistribute the energy among the particles in such a way that the electrons in the pulse front propagate longer than those in the tail by an amount Δt , i.e. the following velocity difference must be induced (follows from $dv/dt = -L_f/t^2$):

$$\Delta v = v^2 \Delta t / L_f \quad (2.11)$$

This translates into energy spread via $dE = mvdv$:

$$\Delta E = \frac{E^{3/2} \Delta t}{L_f} \sqrt{8/m} \quad (2.12)$$

The AC field has a time dependence like $\sin(2\pi\nu t) = \sin(\omega t)$, where $t = 0$ corresponds to the moment when the center of the pulse reaches the center of the cavity. For $\Delta t \ll 1/\nu$ (pulse duration much shorter than one oscillation period), the sine function can be approximated around zero by a linear function, and the new energy spread of the electrons which is created in the cavity can be expressed simply by

$$\Delta E = e\Delta U = eU_{AC}\omega\Delta t \quad (2.13)$$

where U_{AC} is the voltage amplitude of the AC field. One parameter which is not taken into account in this formula is the finite length L_c of the cavity (and with it, the finite transition time $\Delta t_{trans} = L_c/v$), which may lead to an underestimation of the required AC voltage. Actually the particles traveling through a cavity do not acquire the full energy equivalent to the voltage $eU(t)$ (where t is the moment when the particle bunch reaches the cavity volume), but the energy they acquire is reduced by a factor called the transit-time factor Γ ($0 \leq \Gamma \leq 1$) [20]:

$$\Gamma = \frac{\sin(\theta/2)}{\theta/2} \quad \text{with} \quad \theta = \frac{\omega L_c}{v} \quad (2.14)$$

It can be easily verified that this factor also applies to the induced energy spread in our case. This can be explained vividly in the following picture: Electron pulse front and tail spend about the same time in the AC field, and are subject to the time evolution of this field during their transit. The larger the fraction of a complete AC cycle they experience, the smaller the relative net difference in accelerations and decelerations they accumulate, until, for a complete cycle ($\theta = 2\pi$), the difference vanishes, and no energy spread would be induced at all. To account for this fact, eq. (2.13) must be replaced by the following formula:

$$\Delta E = eU_{AC}\omega\Delta t \cdot \Gamma \quad (2.15)$$

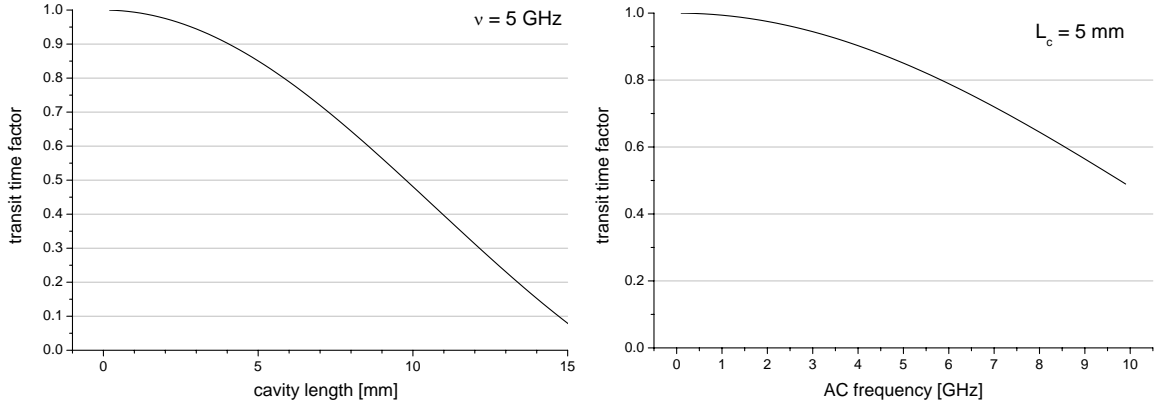


Figure 2.7: Dependence of the transit time factor Γ on the cavity length (for constant frequency of 5 GHz) and the frequency of the AC field (for constant cavity length of 5 mm). Note that $\Gamma = 1$ only for the idealized case of a cavity with zero length or for a constant field (zero frequency).

Using eq. (2.12), one now obtains the required voltage amplitude in the cavity to have the temporal focus at a distance L_f from the cavity:

$$U_{AC} = \frac{E^{3/2}}{\omega e L_f \Gamma} \sqrt{8/m} \quad (2.16)$$

Note that the required voltage is, to first order, not dependent on the pulse length Δt or its original energy spread. However, the condition $\Delta t \ll 1/\nu$ should be fulfilled, otherwise the above approximation of the linearized sine is not valid and a dependence on the pulse length is introduced (because Δt does not cancel out then). And a look at fig. 2.4 makes it clear that if Δt grows beyond $1/2\nu$, the difference in acceleration field between advanced and delayed electrons decreases again, and for $\Delta t > 1/\nu$, the bunching effect even gets reversed and leads to pulse broadening instead of pulse compression.

For an estimation, let $E = 20$ keV, $\omega = 2\pi \cdot 5$ GHz, $L_f = 0.2$ m and $L_c = 5$ mm:

$$\Gamma \approx 0.85 \text{ and } U_{AC} \approx 630 \text{ V}$$

In regard to a feasibility check, the critical question is whether this voltage amplitude can be sustained in a cavity with manageable RF power. This depends on the cavity geometry and the electromagnetic mode that shall be excited. For our purpose, it was found that a so-called pill-box cavity with its TM_{010} mode is best suited [6, 21]: In its simplest form, such a cavity is just a cylindrical volume with metal boundaries, usually made from copper. The frequency ν of the mode is just defined by the radius R_c of the cylinder [20]:

$$\nu = \frac{2.405c}{R_c} \quad (2.17)$$

The length L_c of the cylinder can be chosen arbitrarily and should be kept as short as

possible to maximize the transit time factor (see above). The RF power is dissipated almost exclusively by surface currents on the cavity walls and is then given by [20]

$$P_d = \frac{R_{surf}}{2} \int_S |H|^2 dS \quad (2.18)$$

where R_{surf} is the surface resistance. An approximated expression for the dissipated power in short pill-box cavities is derived in [21]:

$$P_d = 2.76 \cdot 10^{-6} \Omega^{-2} \cdot R_{surf} \left(\frac{U_{AC}}{L_c} \right)^2 R_c^2 \quad (2.19)$$

Note that U_{AC}/L_c is the peak electric field in the cavity. For copper, $R_{surf} = 2.61 \cdot 10^{-7} \sqrt{\omega/\text{Hz}} \Omega$, and a 5 GHz pill-box cavity has a radius of $R_c \approx 23$ mm; inserting the values from above, one obtains

$$P_d = 1.1 \text{ W}$$

Such a power can be handled easily with standard RF devices, and there are even no heat problems to be expected. Thus, from this point of view, the suggested setup is realistic.

One should also consider the absolute extent of the energy spread which is created in the cavity, because actually a sharply defined electron energy is required to attain a high resolution in UED experiments. Combining equations (2.9) and (2.15), one can estimate the energy spread ΔE for the setup parameters suggested on p. 14, an acceleration length $L_a = 10$ mm and an initial energy spread $\varepsilon_i = 1$ eV:

$$\Delta E = \varepsilon_f = eU_{AC}\omega\Gamma\frac{L_a}{E}\sqrt{2m\varepsilon_i} \approx 30 \text{ eV}$$

So the relative uncertainty in energy $\Delta E/E$ is on the order of 10^{-3} , and no severe impact on the UED resolution is to be expected [19].

2.3.2 Synchronization of RF field with pulse timing

As already stated, for optimal bunching the electron pulse has to arrive at the center of the cavity exactly when the AC field goes through zero. If one assumes a symmetric electron distribution inside the bunch with respect to the bunch center, then there is no net energy transfer to the bunch as a whole — some electrons gain a bit of energy, others lose the same amount. A timing error between the electron bunch arrival and the AC field's oscillation has the following consequences:

- The energy spread that the AC field induces on the electron bunch changes.
- A net transfer of energy appears.

It can be found easily that the energy spread which is imposed on the bunch (see eq. (2.15)) is changed to

$$\Delta\tilde{E}(\varphi) = \Delta E \cdot \cos(\varphi) \quad (2.20)$$

where $\varphi = \omega\delta t$ is the phase error resulting from the timing error δt . The bunch's average energy is now

$$\tilde{E}(\varphi) = E + eU_{AC} \sin(\varphi) \quad (2.21)$$

Eq. (2.12) shows the relation between the ‘‘focal length’’ L_f of the temporal lens, the bunch energy and the energy spread induced by the lens. A change in one or even both of the latter results in a different focal length:

$$\tilde{L}_f(\varphi) = \frac{(E + eU_{AC} \sin(\varphi))^{3/2} \Delta t}{\Delta E \cos(\varphi)} \sqrt{8/m} = L_f + \delta L_f \quad (2.22)$$

But in a UED experiment, the target is fixed; it cannot follow a moving location of temporal focus. Even a correction of L_f , e.g. by tuning the cavity voltage, is not possible in the case of a fast jitter in φ (unless there is an extremely fast real-time feedback from a pulse length measurement at a fixed location near the target, which is probably not feasible). Therefore, let us estimate the electron pulse length which the target experiences when L_f has shifted by a small amount δL_f .

For correct timing, a pulse arriving at the temporal lens with duration τ compresses, to first order, to zero while it propagates a distance L_f , so $d\tau(L)/dL = \tau/L_f$. Denoting the pulse length at the target location with τ_t such that $\tau_t(L_f) = 0$, one gets for small deviations δL_f from the optimum focal length:

$$\tau_t(\tilde{L}_f) = \tau \left| \frac{\delta L_f}{L_f} \right| \quad (2.23)$$

Using eq. (2.22) and a first-order Taylor expansion for the power of 3/2, one arrives at the following dependence on the phase (or timing) error:

$$\tau_t(\varphi) = \tau \left| \frac{1}{\cos(\varphi)} \left(1 + \frac{3U_{AC} \sin(\varphi)}{2U} \right) - 1 \right| \quad (2.24)$$

A comparison with GPT simulations shows that this formula constitutes a satisfactory approximation (see fig. 3.8 on page 24). Putting realistic numbers into the equation, it is remarkable that even a timing error of a few picoseconds is tolerable. So the AC field must be synchronized to the electron pulse repetition rate, and therefore to the laser pulse repetition rate, with an error of about a picosecond, which corresponds to the jitter of the laser available for this project². Locking of a passively mode-locked

²S. Naumov, A. Apolonskiy (unpublished)

laser to an RF source has already been demonstrated with a timing jitter of even less than 10 fs [22]. One can conclude that it should be possible to achieve the required timing precision.

2.4 The role of the photoelectron energy distribution

It is worthwhile to discuss the initial energy spread ε_i in the electron bunch at the moment of its emission from the cathode, since this is one of the key parameters that determine the attainable pulse duration. For a simple electron gun without bunching, it holds for the pulse length τ (see eqs. (2.9), (2.10)):

$$\tau \propto \sqrt{\varepsilon_i} \quad (2.25)$$

If bunching is applied, then one has for the minimum pulse length τ_f in the temporal focus (see eq. (2.4)):

$$\tau_f \propto \varepsilon_i \quad (2.26)$$

Both relations are supported by simulations, see chapter 3. So if one wants to go to ultrashort electron pulses, one has to care about this quantity ε_i . But by what is this variable determined physically? It is just the excess energy from the photoemission process that the electron keeps in the form of kinetic energy. In the most simple model, the photoemission looks as follows:

The electrons in the cathode material are confined into the metal by a potential barrier to the vacuum, the work function W . Photons from the laser radiation transfer energy to an electron in a quantized manner, and the energy amount is $nh\nu$, h being the Planck constant, ν the light frequency, and n the number of photons per single electron, since it may be a multiphoton process. So the kinetic energy the electron carries after its emission is the excess energy

$$E = nh\nu - W \quad (2.27)$$

Obviously, this is a strongly simplified model. In reality, the photoelectrons do not all have this distinct energy; instead they have an energy distribution of finite width due to the following reasons:

- finite energy distribution of electrons inside the metal
- uncertainty in photon frequency (finite spectral width of the laser pulse)
- above-threshold photoemission (ATP) possible for high laser intensities

Inside the metal, the quasi-free electron gas has a Fermi-Dirac distribution in energy, where the idealized sharp energy cutoff at the work function is smeared out in an interval dependent on the material's temperature. The spectral width of the laser

pulse does not contribute significantly to the electron energy spread³, whereas ATP processes lead to photoelectron energies that may lie several photon energies above the expected excess energy from eq. (2.27).

An experimental investigation of the matter, with parameters relevant to this work (like laser pulse lengths below 100 fs), was done by M. Aeschlimann et al. [23]. They found that especially for multiphoton photoemission, the spectra of the emitted electrons can have much larger widths than one would naïvely expect, and that ATP processes are not always negligible. For instance, if the photoeffect for the given light frequency requires at least three photons per electron, a high incident laser intensity is needed to outbalance the vastly reduced efficiency for such a high-order process. Due to this high light intensity, even higher-order interactions become probable enough to broaden the photoelectron energy distribution significantly by ATP. Furthermore, a high laser intensity may lead to a localized strong temperature increase, which also broadens the range of energies from which the electrons inside the metal can be released into the vacuum. This is not necessarily connected to a heating of the whole material (the lattice), but during the laser pulse duration, a very short-lived but very pronounced peak in the electron gas temperature could occur, because the laser pulses are shorter than typical electron-lattice relaxation times.

The results of M. Aeschlimann’s working group which are most relevant here are presented in fig. 2.8. They used a mode-locked titanium:sapphire laser with a tunable wavelength output from 750–850 nm, producing pulses with 70–90 fs of duration and about 10 nJ of energy at a repetition rate of roughly 80 MHz. So apart from the fact that we could produce pulses with higher energy, these values reflect our conditions quite well. The work function of copper is about 4.5–4.65 eV, depending on the orientation of the crystal axes, so they needed at least three photons of their fundamental light frequency to release one electron from the material. They compared this scenario with the cases of frequency-doubled photons (2-photon-photoemission) and frequency-tripled photons (1-photon-photoemission). Fig. 2.8 shows (from left to right) 1-photon-, 2-photon- and multi-photon-photoemission.

It is striking that with increasing order of the photoelectric effect, the energy distribution of the freed electrons gets significantly broader. The rightmost plot shows a spectrum which extends more than 5 eV above the emission threshold, which is several photon energies *more* than to expect. This phenomenon may be explained by ATP, possibly in combination with an extreme short-lived heating of the electron gas in the solid during the relatively intense laser pulse, but a detailed explanation goes beyond the scope of this thesis. The important point is the clear tendency towards lower photoelectron energy spreads for lower-order photoemission processes.

However, there are some remarks to be made. Firstly, as the focus of the cited work lay in the quantitative details of the photoemission process, the vacuum conditions were much better than in our case, and specially cleaned mono-crystal samples of copper were used. Nevertheless, the qualitative results should be transferable to our photocathodes, at least for copper, and maybe also for gold, which behaves similar to copper with respect to the photoelectric effect. Secondly, it is worth to point out that

³The uncertainty in photon energy for our experimental conditions, a 40 nm wide spectrum around 800 nm wavelength, is only 0.07 eV.

the reported energy spreads were not affected by space-charge effects (electron-electron repulsion), because the laser intensity was always kept so low that the average number of emitted electrons per laser pulse was one.

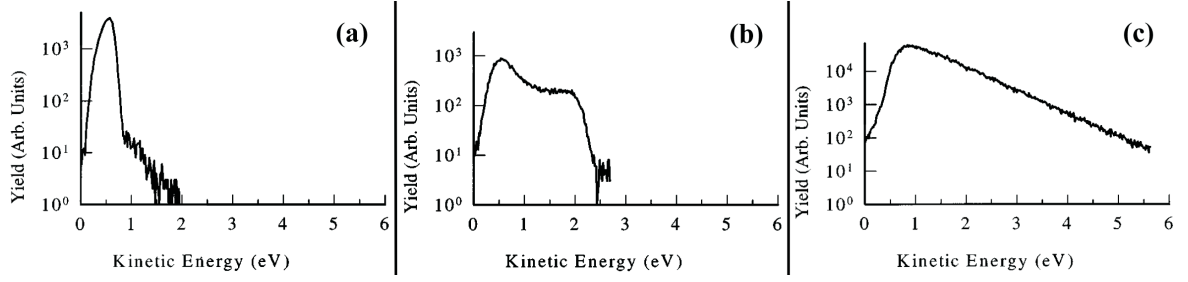


Figure 2.8: Measurement results from [23]: Shown are photoelectron spectra in eV for the case of (a) single-photon, (b) double-photon, (c) multi-photon photoemission. The peak laser intensities were $1 \cdot 10^4 \text{ W/cm}^2$, $1 \cdot 10^7 \text{ W/cm}^2$ and $1 \cdot 10^9 \text{ W/cm}^2$, respectively. (*Figures reproduced with the authors' permission*)

The essence of these findings, regarding our experimental work, is basically the following: To minimize the photoelectron energy spread, one has to try different light frequencies and probably go to frequency-doubling or -tripling in order to have low-order photoemission processes. Additionally, the cathode material should be carefully chosen in such a way that its work function is as close to the photon energy (or an integer multiple of it) as possible, to have an intrinsically low excess energy. However, selecting the best-suited cathode material is not a trivial task, because it is deposited as a thin film on a silica substrate (see section 2.1), and the work functions of such thin metal layers are not known a priori. They often differ significantly from the values for bulk material [24], which also supposes that there is a strong dependence on the precise thickness of the layer, and it is well-known in surface physics that surface contaminations can have a vast impact on the work function as well. From the values presented in the above-cited article, we can assume a work function around 4 eV. Another issue in choosing the cathode material are practical criteria like chemical stability of the material and lifetime of the cathode.

For this reason, the experimental work was focused on driving the electron gun with different light frequencies and comparing two easily manageable cathode materials: gold and copper. Furthermore, measurements were done to estimate the initial energy spread of the photoelectrons. All those efforts constitute important preparatory work for the future ultrashort electron pulse source.

Chapter 3

Computer simulations

The behavior of the electron beam was simulated numerically to check results from analytical estimations and to gain further insight into some details that would have been more elaborate to work out analytically. So in most cases, the simulations were employed for feasibility studies for the ultrashort electron pulse generation, but sometimes they also proved convenient in order to understand the behavior observed in the experiment.

3.1 The simulation system

For all simulations of the electron gun, the General Particle Tracer (GPT) software was used, a commercial tool specializing in accelerator and particle beam line design [25]. The code tracks every single particle and solves the relativistic equations of motion with a fifth order Runge-Kutta algorithm with adaptive timestep size control for increased precision. The source code of the Runge-Kutta driver is not accessible, but the beam line components like apertures and any static or time-dependent electromagnetic fields are described in an input file by a collection of simple commands, providing models for many common accelerator structures and allowing to import arbitrary field configurations computed by third-party software. The initial particle distributions in space, energy, etc. can be defined in this file as well, and certain accuracy limits or timestep sizes can be enforced. Complete particle data sets for a specified series of either times or spatial locations are stored in special database files, permitting any possible representation of the dynamics afterwards, either for all single particles or in the form of statistics. Inter-particle interactions are accounted for by several different space-charge models, from simplified versions relying on symmetries or other assumptions to full 3D versions. The space-charge effects can also be disabled in order to simulate purely ballistic motion. Scattering at potentials or at solid structures is supported.

3.2 Modeling the setup

All simulations were based on the following scenario (x , y , z are the Cartesian coordinates, the z axis corresponding to the beam axis, t is time):

- A bunch of n electrons starts around $z = 0$ with a Gaussian distribution in z of standard deviation 25 nm (to account for the finite cathode material thickness) and around $t = 0$ with a Gaussian distribution in time of standard deviation $\tau_i/2$ (to account for the finite laser pulse duration).
- In radial direction, the particles have a Gaussian distribution in x and y (i.e. a Gaussian beam profile) with a standard deviation (initial beam radius) r_0 .
- The initial momentum distribution is isotropic.
- The energy distribution of the bunch is a truncated Gaussian with an FWHM (full width at half maximum) of $2\varepsilon_i$, such that the peak of the Gaussian, i.e. the highest probability, is at zero energy, see fig. 3.1. Hence, the characteristic width is the HWHM (half width at half maximum) of ε_i . To be precise, in GPT one cannot define the energy distribution directly, but only the distribution in Lorentz factor γ , but since $\gamma \approx 1 + E/mc^2$ (E the kinetic energy) and $d\gamma = dE/mc^2$, this transforms linearly into an energy distribution.
- At first, the particles are accelerated in positive z direction in a static field, whose strength is given by the potential difference $U = 20$ kV divided by the length of the DC acceleration stage, L_a (usually 10 mm). The static field is either chosen as completely homogeneous (to approximate the case of a mesh anode, where the large grid area acts nearly as a continuous plane of defined potential, producing a nearly homogeneous field) or the field has an inhomogeneity at the anode location, mimicking the field distribution at a conducting surface with a hole (corresponding to the metal anode with just one circular aperture for the beam). It is also taken into account that electrons which are too far off-axis hit the metal instead of passing the hole — they are effectively removed from the simulation upon hitting the virtual solid surface. The hole radius R_h is usually 0.5 mm, as it was the case in the real setup.
- Behind the anode region, the particles propagate freely. Only if the bunching process is simulated as well, the particles enter the time-dependent field of the TM_{010} mode of a cylindrical RF cavity after passing the anode. The mode has a frequency ν and a voltage amplitude U_{AC} . The inner cavity volume (containing the AC field) begins 5 mm behind the anode (to account for a finite wall thickness of the cavity) and extends over a length of another 5 mm. Behind this region, the electron bunch propagates freely again.
- If not specified otherwise, space-charge effects were switched *off* to account for the fact that we expect only about one electron per pulse. Of course, for the simulation to provide useful statistics, it is necessary to run it with hundreds of particles at once — this is equivalent to running many single-particle pulse simulations at the same time and collecting the statistics afterwards.

(Remark: For all simulation results presented in this thesis, the above-mentioned parameters are given. If some parameters are not listed, then they were equal to their default values specified above. If the accelerating field was assumed to be fully homogeneous, this is indicated by a note “hom. field”.)

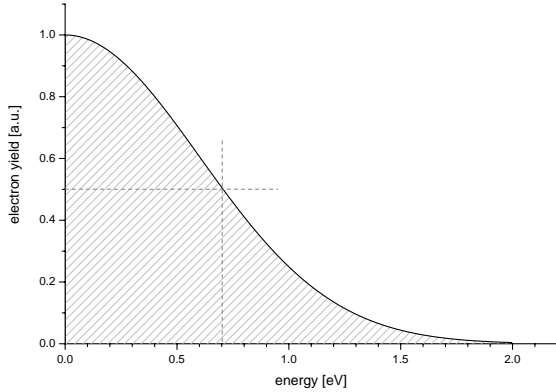


Figure 3.1: Truncated Gaussian with a HWHM of 0.7 eV. This is a typical particle energy spectrum used in the simulations, for parameter $\varepsilon_i = 0.7$ eV.

The electrons’ initial energy distribution in the simulations is not equivalent to a Maxwell-Boltzmann distribution for which you could define a *temperature*, because it does not fall off exponentially with E , but exponentially with E^2 . As can be seen from the results in [23], shown in fig. 2.8, real photoelectron spectra mostly have a rather steep descent for increasing energy (note that the scales in the figure are logarithmic). For this reason, the above mentioned model distribution was chosen. The maximum of the Gaussian was placed at energy zero, to represent a photoemission process with ideally chosen photon energy exactly equal to the work function of the cathode material, so that there is no excess energy left from the photon which could shift the distribution’s peak towards an energy above zero.

In the following section, some simulation results are shown which either confirm the theory presented in the preceding chapter, or make aware of additional effects which the simple theory does not take into account.

3.3 Selected simulation results

3.3.1 Evolution of electron pulse length

The first interesting point to examine is, of course, the evolution of the electron pulse length in time, or in space along the beam axis (z axis), respectively. As a measure of electron pulse length, the doubled standard deviation (square root of the second moment) of the particles' distribution in time was used. Actually the only straightforward means of bunch length determination offered by GPT was the standard deviation of the spatial particle distribution in the bunch, and by dividing the resulting spatial length by the mean velocity (20 keV of kinetic energy correspond to $8.1 \cdot 10^7$ m/s) and multiplying by two, the pulse duration was obtained. Therefore it is sometimes referred to as "second-moment pulse length".

A typical pulse length evolution is shown in fig. 3.2. After its release of the electron bunch from the cathode material, triggered by the laser pulse, its length grows rapidly during the acceleration process. This fast bunch expansion comes to a halt as soon as it leaves the DC field, after the first 10 mm. One can see a free propagation over 5 mm, then the bunch enters the cavity (a first sign of bunching is visible, because a part of the necessary energy spread is already imposed on the electrons). After the transit through the cavity (another 5 mm), upon leaving the AC field, the remaining part of the energy spread becomes manifest, and the pulse length starts to decrease linearly, until the point of temporal focus is reached, where the pulse length is minimal and then increases again, with the same slope with which it decreased before. This symmetry can be attributed to time inversion symmetry in the temporal focusing (at least in the absence of space charge): The relative speed with which some particles in the bunch overtake the others does not change if all velocities are reversed.

Note that, for our parameter range, the pulse duration increases to values of several hundred femtoseconds during the DC acceleration, which means that the initial pulse duration τ_i (which can only be as long as the laser pulse at the utmost, i.e. below 100 fs) is not a very critical parameter. The main contribution to the electron pulse length, at the point when it leaves the accelerating field, develops from the particles' initial energy differences. This fact is illustrated in fig. 3.3, where the simulated electron pulse duration behind the acceleration stage is plotted for different amounts of initial energy spread (from an unrealistically low value of 0.01 eV up to 1 eV). The data points match quite well to a square root function, as one would expect from eq. (2.9) (p. 12). A deviation from the square root function is only visible for extremely small energy spreads, where the contribution from the temporal aberration (τ_i) gets dominant. The model used in those simulations contained no RF cavity, so the pulse lengths presented are those one would obtain in a simple electron gun with pure DC acceleration. Without bunching and in absence of space-charge effects, the pulse length stays quite constant during further propagation.

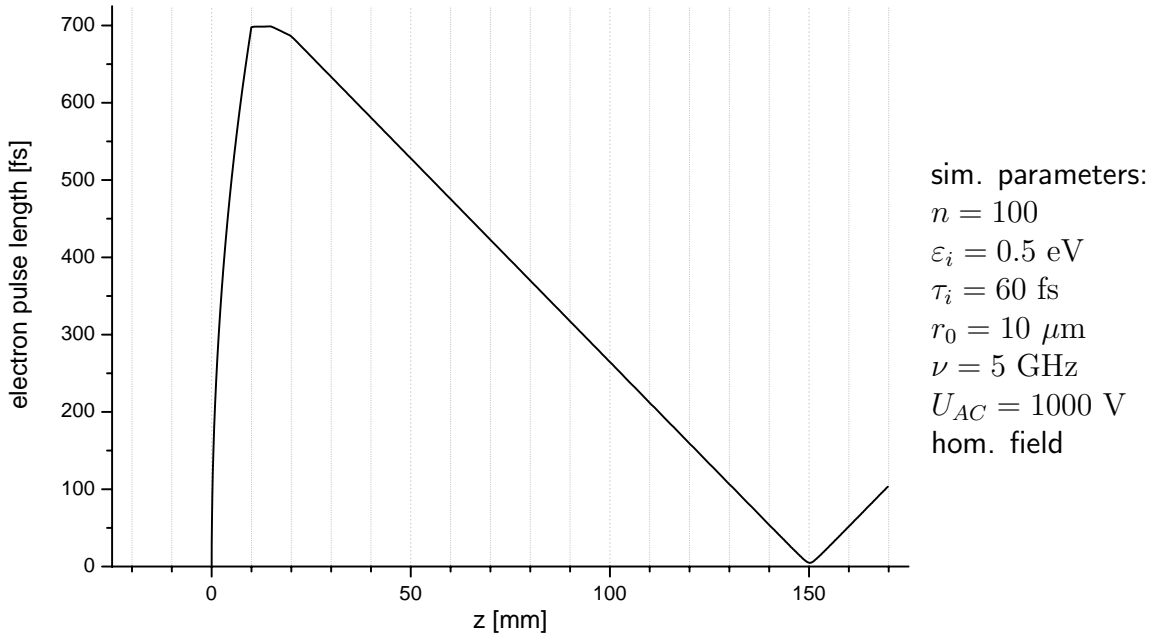


Figure 3.2: Evolution of the electron pulse length in an electron gun with a bunching cavity: 2nd moment electron pulse length versus spatial coordinate z .

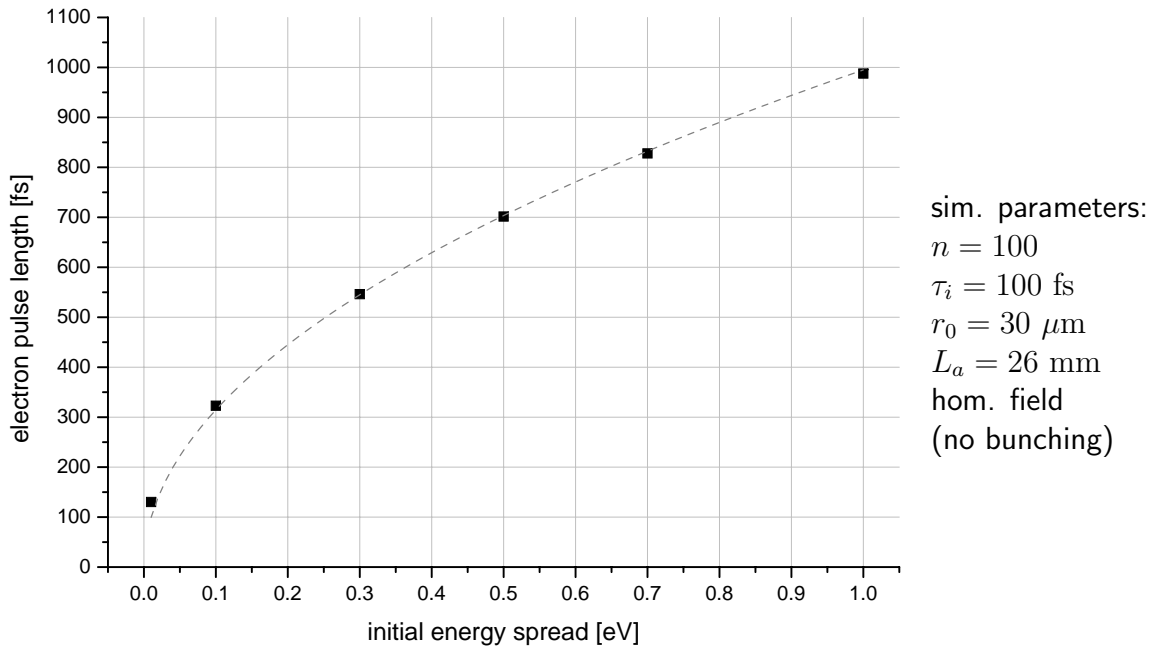


Figure 3.3: Duration of the electron pulse upon leaving the accelerating DC field, for different initial energy spreads of the bunch (black). The dependency largely follows a square root function (gray).

Now that the decisive role of the initial energy spread is ascertained, the next logical question is how the temporally focused electron pulse length depends on that quantity, i.e. how short the pulses can get after bunching. The answer is already provided in eq. (2.4) (p. 11), but it is supported again by the simulation data presented in fig. 3.4, reflecting the linear correlation.

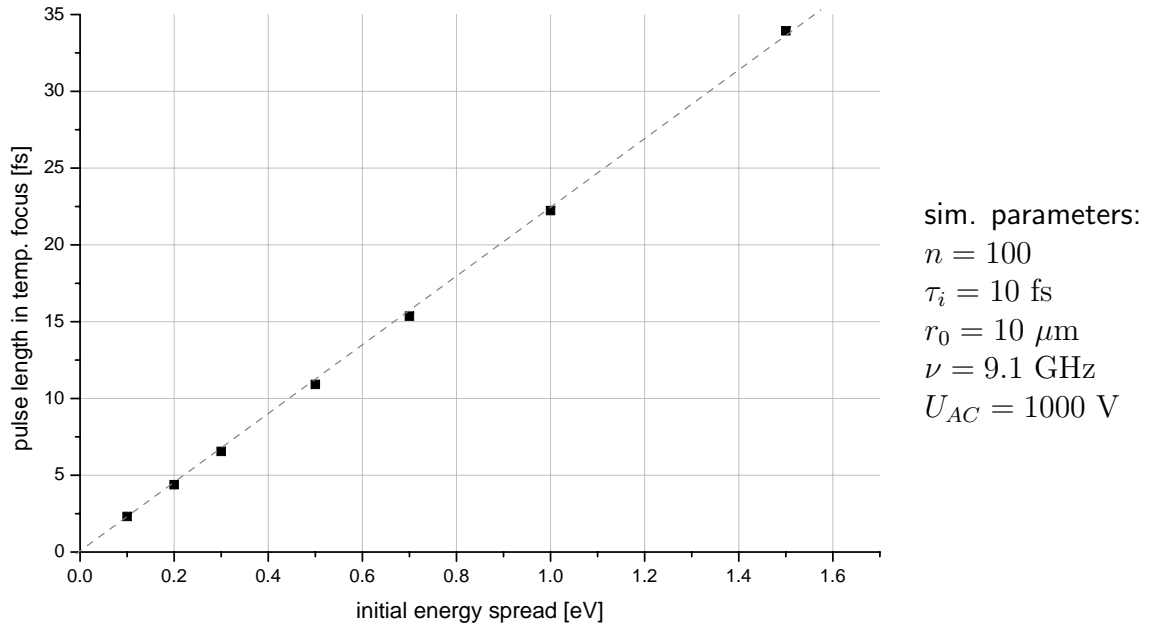


Figure 3.4: Duration of the electron pulse achieved at the point of temporal focus, for different initial energy spreads of the bunch (black). The dependency is linear, in contrast to the correlation shown in fig. 3.3.

3.3.2 Space-charge

Even if the average number of electrons per bunch can be kept around one, it would be desirable for UED experiments to be able to increase the beam current (and hence, the signal on the detector) without a significant trade-off in electron pulse length: E.g. an increase in beam current by a factor of 10 reduces the integration time necessary to obtain the diffraction image by the same factor. Therefore, it is advisable to have at least a short look on the effects of space-charge. This problem is hard to tackle theoretically, whereas simulations are a means of investigation which is both easy and reliable.

Fig. 3.5 shows, in the upper half, a comparison of how the electron bunch lengths evolve in the range of temporal focus. For those simulations, it was ensured that the *transversal* distances between the particles remained small in order to have a rather pessimistic scenario where the inter-particle forces are strong enough to affect the bunch length significantly. So a rather small initial beam radius and a small initial energy spread were assumed. The evolution of the beam radius (taken as standard deviation of the transverse coordinates) is shown in the lower half of the designated figure. Even at the target (temporal focus) location it stays below $140\ \mu\text{m}$ — this is in the order of magnitude which is given as the electron beam radius at the target in existing UED setups (see, e.g. [3], p.1787), and mostly those beams have a larger initial divergence and are then refocused, whereas in the simulations shown here the beam stays narrow and the time-averaged distance of the electrons is lower. For the RF voltage a high value was chosen to have a very efficient bunching, which again brings the electrons very close together in the focal point, now in longitudinal dimension.

It was found that even a few tens of electrons per pulse did not have a severe effect on the bunching. By space-charge, the minimum pulse duration is increased by one or a few femtoseconds, and the point of temporal focus, where this minimum appears, is shifted a few millimeters towards larger distances. In a UED experiment, this spatial shift could already push the temporal focus out of the thin target volume, but even if the pulse duration is evaluated at a *fixed* optimum location on the z axis (at $z = 83\ \text{mm}$ in the example), the pulse length is still not increased above 20 fs. It is therefore permitted to omit them in both the simulations and the analytic model.

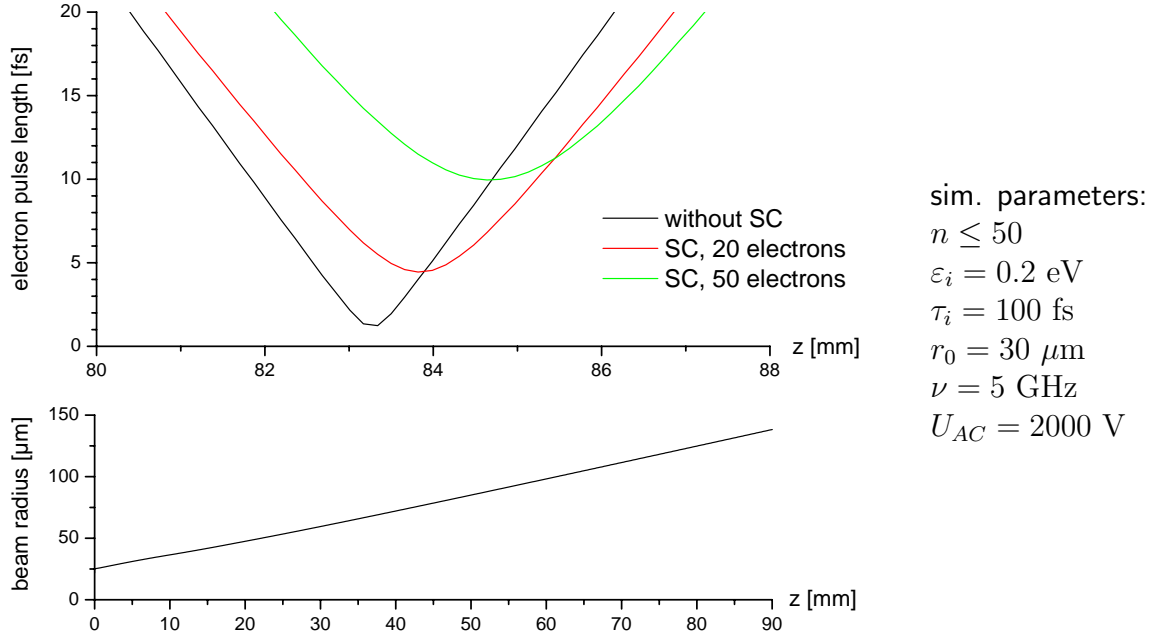


Figure 3.5: The impact of space-charge effects on temporal focusing (upper plot): The goal is to have single-electron pulses (black graph), but even with a few tens of electrons per pulse (colored graphs) the pulse duration stays well below 10 fs. The beam radius (lower plot) remains small during the whole propagation, making sure that the electrons are not distributed over a too large bunch volume.

3.3.3 Electric field inhomogeneities at the anode

One of the more surprising findings was that the inhomogeneity of the electric field at the anode's hole is not negligible. As can be seen in fig. 3.6, the hole leads to a field configuration which results in radial accelerations, effectively defocusing the electron beam. Another more serious consequence of this spatial bunch deformation is the fact that the temporal focusing mechanism is disturbed, due to the following reason: In the field inhomogeneity, all electrons which do not go exactly through the center of the hole, but a bit off-axis, acquire velocity components perpendicular to the beam direction, so a part of their kinetic energy is carried in transverse velocity, which means they have a slight lack of longitudinal energy. Because the RF cavity is situated closely behind the hole, this newly emerged deficit in longitudinal energy does hardly become manifest as a delay in arrival time, so the time-dependent electric field does not compensate for this effect. As a result, the off-axis electrons fall behind the centered electrons during further propagation, and the pulse duration at the temporal focus is increased.

This was one of the peculiarities that were found only in the simulations, because a simple 1-dimensional analytical treatment like in section 2.3 cannot reveal this effect. A more detailed analysis of the phenomenon is carried out in [19] and a simple solution to the problem is presented. However, the effect should be avoidable in the first place by employing a fine-meshed metal grid as anode instead of a simple metal aperture.

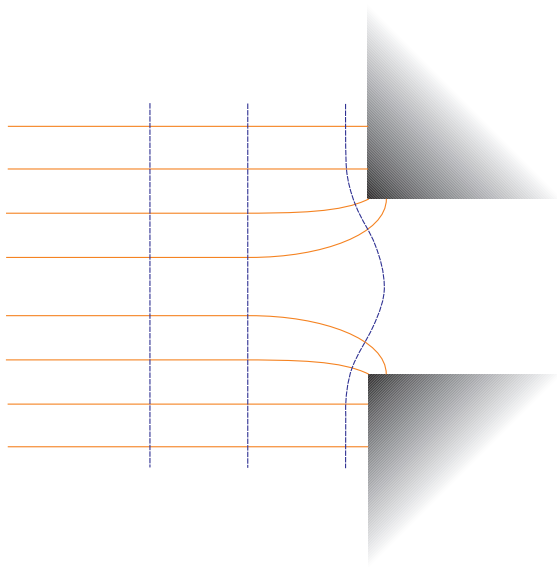


Figure 3.6: Electric field in the vicinity of the hole in the anode metal: z axis points to the right, electron beam enters the hole (shown in a lateral cut) from the left. Red lines represent electric field lines, blue lines indicate equipotential surfaces. It is obvious that the field deformation leads to transverse velocity components for off-axis electrons, since the acceleration is in the direction of the field lines.

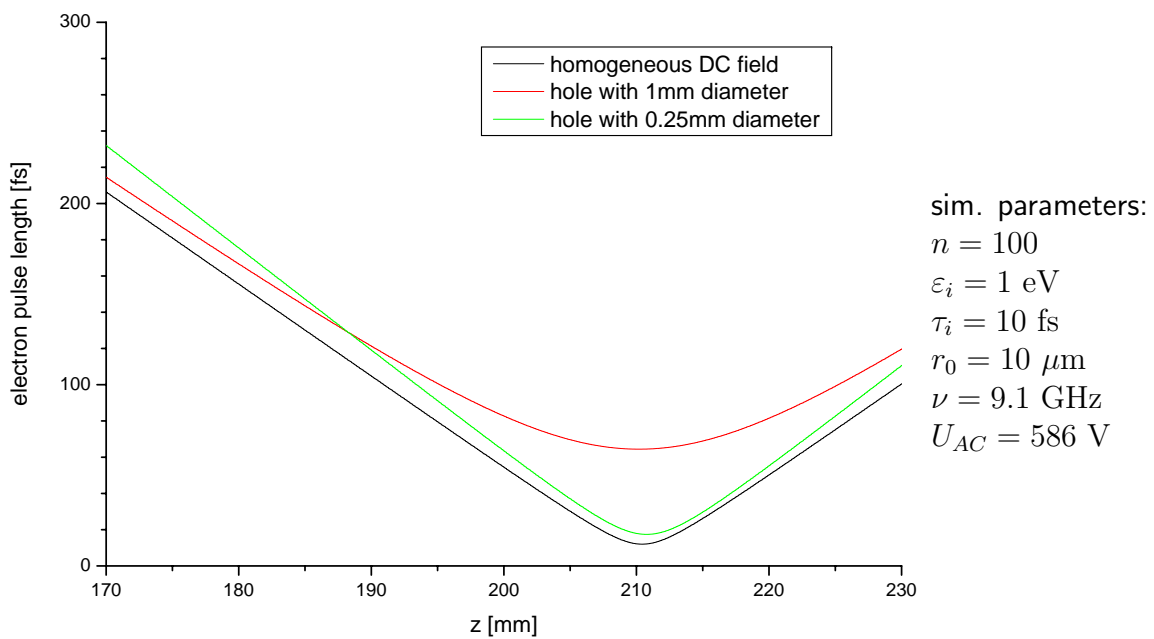


Figure 3.7: Demonstration of the distortion effect of the small electric field inhomogeneity at an anode which consists only of a flat grounded metal surface with a hole as a beam aperture: A hole with 1 mm diameter already leads to a much weaker pulse compression (red) than in the case of an ideal homogeneous acceleration field (black). The distortion is less pronounced for smaller holes.

3.3.4 Timing errors of the AC field with respect to electron arrival

In section 2.3.2 a formula was derived to estimate the effects of an error in synchronization between electron pulse arrival and phase of the AC field in the bunching cavity (eq. (2.24), p. 16). Fig. 3.8 shows a comparison of that formula with GPT simulations. The two dips in the theoretical curve going down to absolutely zero are not realistic, of course, as can be seen in the simulated data: In the model developed in section 2.3.2, higher-order effects are not taken into account, but they are the reason why the pulse duration never reaches zero (see again eq. (2.4), p. 11).

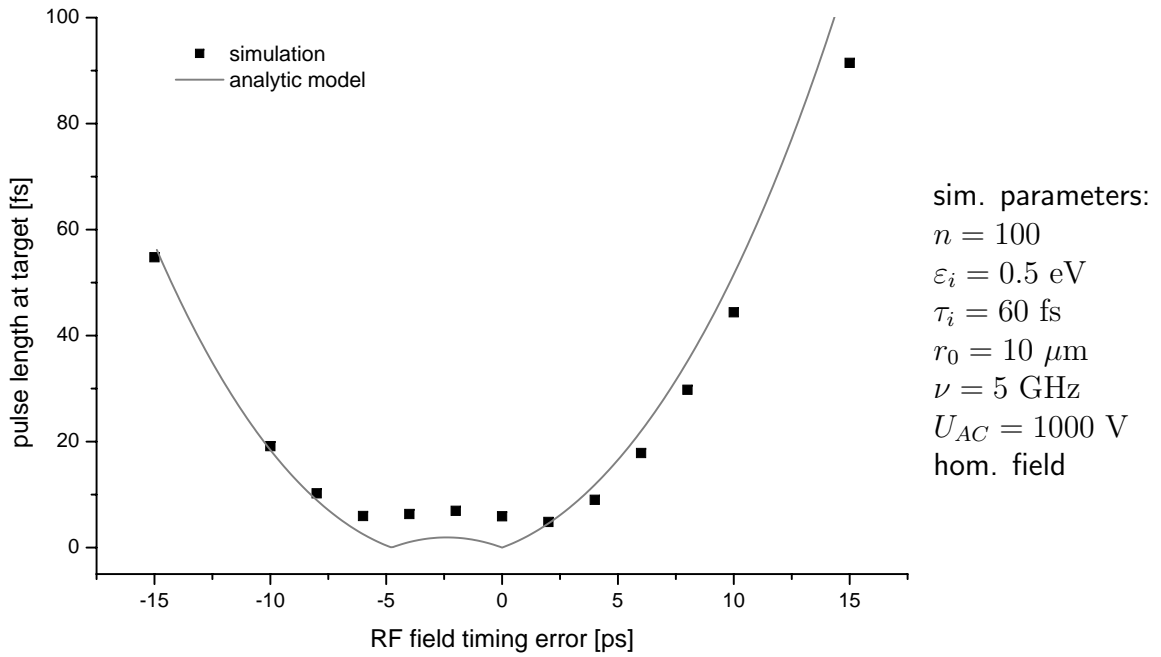


Figure 3.8: Electron pulse duration at a *fixed* (target) location as a function of timing error between pulse arrival and AC field oscillation in the RF cavity.

Chapter 4

Experimental work

4.1 Experimental setup and methods

4.1.1 The laser system

The femtosecond laser pulse source which was used to drive the electron gun is described extensively in [5, 26]. Therefore I only describe the most important details in the following.

The laser is a titanium:sapphire-based passively mode-locked oscillator. Its most outstanding feature is its combination of a pulse repetition rate of 2.8 MHz with a high pulse energy of about 300 — 400 nJ without any post-amplification (so the average power is about 1 W). Such a high pulse energy is necessary to attain a high enough electron yield from the gun's cathode in a first stage of the project, and later, those pulses have to be able to deliver even enough energy for pumping in pump-probe UED experiments, after their passage through a double-pass amplifier.

The high pulse energy is possible only because the system operates in the so-called positive-dispersion regime (PDR), as opposed to the more common negative-dispersion or soliton regime (NDR). These terms describe the type of intracavity group delay dispersion (GDD) which dictates the pulse evolution inside the laser cavity.

For an explanation, let us have a look at the dispersion relation of lightwaves with wavelength λ , wavenumber $k = 2\pi/\lambda$ and angular frequency ω in dispersive media:

$$k(\omega) = k(\omega_0) + \left. \frac{\partial k}{\partial \omega} \right|_{\omega_0} (\omega - \omega_0) + \frac{1}{2} \left. \frac{\partial^2 k}{\partial \omega^2} \right|_{\omega_0} (\omega - \omega_0)^2 + \dots \quad (4.1)$$

This is actually just a Taylor expansion of $k(\omega)$ around a frequency ω_0 , which is, for a laser pulse, the center frequency of its spectrum (carrier frequency). The first derivative $k' = \partial k / \partial \omega$ defines how k , or the wavelength, changes with frequency to first order, therefore it is called first-order dispersion. It is shown in any textbook on optics

that this derivative is equal to the inverse group velocity, $1/v_g$. The group velocity is the speed of propagation of the peak of a narrow-band optical pulse. A broad-band optical pulse, such as an ultrashort laser pulse, can be thought of as consisting of many narrow-band pulses with different center frequencies, where the contribution of these center frequencies to the whole pulse is given by the pulse spectrum. Thus, the second derivative $k'' = \partial^2 k / \partial \omega^2$ gets important, which defines how the group velocity (or actually the inverse group velocity) changes with frequency. This is called second-order dispersion or group velocity dispersion (GVD), which is nothing else than the group delay dispersion *per unit length*. The GVD is usually given in units of fs^2/cm and is a property of a material (medium), whereas GDD is a property of a given optical path (e.g. a specific laser resonator) along which the light has to propagate through defined lengths of certain media, and is given in fs^2 .

Most transparent media exhibit so-called “normal dispersion”, which means $k'' > 0$, so an initially unchirped laser pulse propagating through a normally dispersive medium broadens in time and acquires a positive chirp: the higher-frequency components of the pulse have a lower group velocity (because $k'' > 0$ is equivalent to $\partial v_g / \partial \omega < 0$) and become more and more delayed with respect to the lower-frequency components. I.e. when this laser pulse passes a certain point in space, the light frequency measured at this point does not stay constant during the duration of the pulse, but first the lowest frequencies are detected, then the center frequency arrives and finally the highest frequency components appear. This time-dependence of the “instantaneous frequency” $\omega_i(t)$ within a laser pulse is called chirp, and the chirp is positive if $d\omega_i/dt > 0$ (see fig. 4.1). A laser pulse has its minimum duration when it has zero chirp, i.e. no frequency components are delayed with respect to others. The larger the chirp, the longer the pulse — but a long pulse with large chirp has the potential (enough spectral width) to be compressed to a much shorter duration if the delays between all the frequency components can be eliminated.

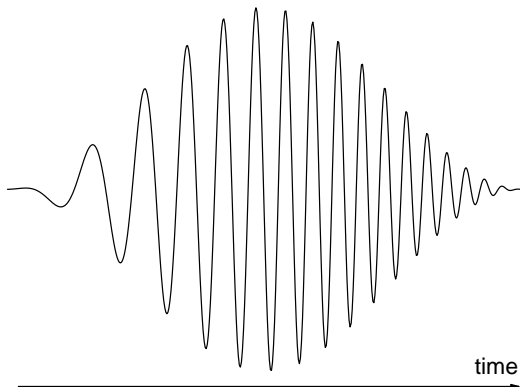


Figure 4.1: Example of a positively chirped laser pulse (electric field vs. time): Higher frequencies are delayed (shifted rightwards).

Let us now come back to the laser systems: Most femtosecond oscillators are designed in such a way that the laser pulses exist as solitons inside the optical cavity, i.e. their natural broadening due to the normal dispersion in air and the glass of lenses, prisms etc. is counterbalanced by negatively dispersive elements inside the cavity. In each roundtrip, all amounts of chirp that the pulse acquires while it passes through dispersive media are compensated by passing those correction elements, e.g. chirped mirrors. Usually the cavity even has a net negative GDD, i.e. it is kept in the negative dispersion regime. The advantage of such a design is that the laser directly produces

ultrashort bandwidth-limited pulses, i.e. the pulses are as short as it is possible with their given spectral width when they reach the experiment.

Our oscillator works in the positive dispersion regime. In the PDR, the pulses are not compressed, but even stretched further inside the optical cavity, which means they have a duration of one or several picoseconds — this allows for much higher energy per pulse. Since the energy is distributed over a larger duration in time, the peak power is much lower, and the pulse as a whole can contain much more energy without reaching the limit in peak power which is given by unwanted non-linear effects. Still, the pulses have a broad enough spectrum to be post-compressed to durations below 100 fs once they have left the resonator. This is one of the strategies how to achieve several hundred nJ of pulse energy.

Another important property which makes the high pulse energy possible is the low repetition rate on the order of a few MHz. Its advantage is illustrated in fig. 4.2. A low pulse repetition rate allows for a long build-up time of the population inversion of the involved energy levels in the laser gain medium (sapphire crystal), to a considerably higher value. Consequently, a larger number of photons can add to the pulse by stimulated emission in every roundtrip, and the equilibrium between gain and losses in intracavity laser power can be maintained at a higher power level. The sapphire crystal was pumped with a wavelength of 532 nm and a power around 8 W.

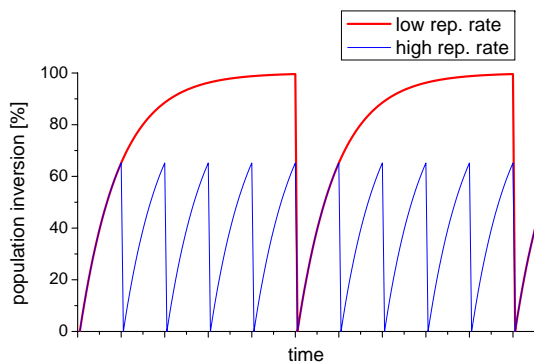


Figure 4.2: Time evolution of the population inversion in the laser gain medium of an oscillator. By permanent pumping, the inversion increases and eventually saturates, but every time the intracavity laser pulse passes through the medium, the population of the upper level is suddenly depleted due to stimulated emission. A low pulse repetition rate (red) allows for much higher population inversion, hence for higher pulse energies, than a high repetition rate (blue).

The low pulse repetition rate of the oscillator was achieved by incorporating two multi-pass Herriott cells into the cavity. Such a cell is basically a telescope which preserves the q -parameter of the laser beam, while it extends the spatial length of the resonator by a great amount [27, 28]. A larger resonator length means a larger roundtrip time for the pulses, and hence a lower repetition rate. One mirror of such a telescope is flat, while the other one is slightly concave, to compensate for the beam divergence such that all important beam characteristics (like its radius) are preserved.

The mode-locking in the oscillator is based primarily on saturable absorption. One of the end mirrors of the laser cavity is a semiconductor Bragg reflector (SBR) which acts as a saturable absorber. To explain it in the most simple picture, the mode-locking and pulse-shaping works in a way that low light intensities are suppressed (because they are absorbed), whereas high intensities are reflected from the SBR and fed back into the resonator. Following an evolution principle, out of initial power fluctuations only the peaks survive and get enhanced — pulses build up. In practice, initiating this

kind of mode-locking was very simple, since only a slight mechanical perturbation in the CW mode (a gentle push on the SBR, or even just closing the laser's housing) was needed.

The resonator design of the laser in its latest configuration, as it was used for this thesis, is shown in fig. 4.3 (There are minor differences in comparison to the configuration shown in [5]). The cavity length is approximately 50 m, folded onto a breadboard which is just 1.2 m in length and 0.6 m in width. The beam quality was determined by a measurement of collimated beam diameter and beam size in a focus, resulting in an M^2 -value [29] of about 1.3. The unfocused beam diameter amounted to about 2.5 mm. The spectrum was not Gaussian, but rather of the rectangular type, with a width of 40 – 50 nm centered around 800 nm in wavelength (see fig. 4.5). Fig. 4.6 shows an example of an autocorrelation signal as it could be attained with such spectra.

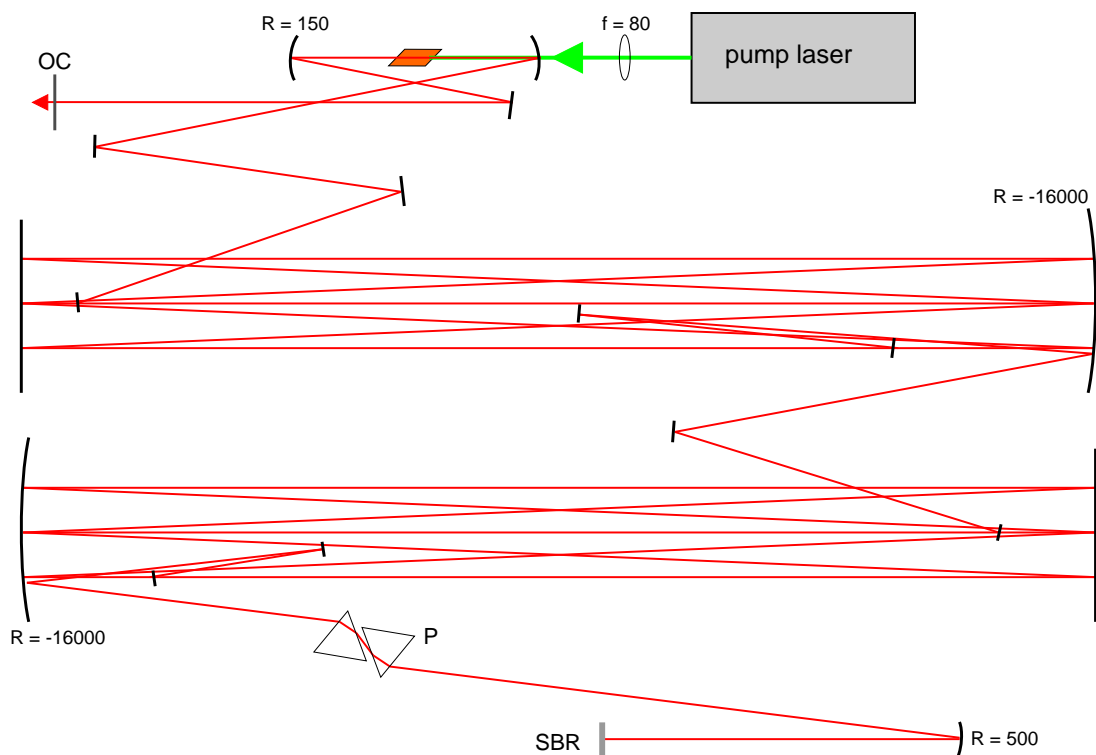


Figure 4.3: Resonator design of the 2.8 MHz Ti:Sa oscillator: (OC) output coupler, (SBR) saturable Bragg reflector, (P) prism pair for intracavity dispersion control (one of the prisms translatable). The pump laser is a *Verdi V-10* from Coherent. All values are in mm. For the sake of clarity, the optical path inside the multi-pass cells is only shown symbolically; actually there are 10 to 12 reflections on each end mirror of each telescope.

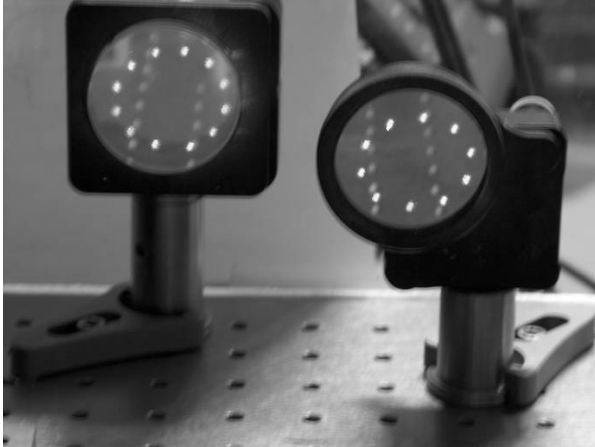


Figure 4.4: End mirrors of the Herriott cell with their multiple reflections arranged in circles.

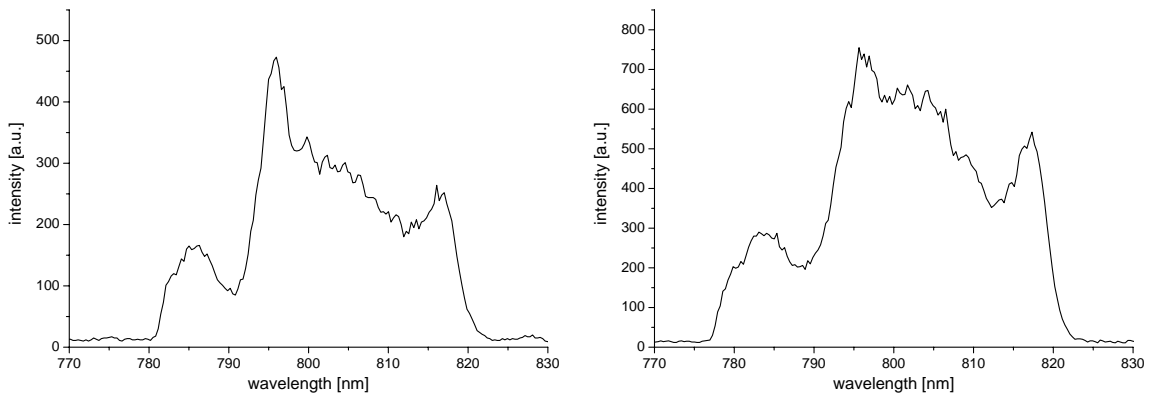


Figure 4.5: Typical spectra of the oscillator.

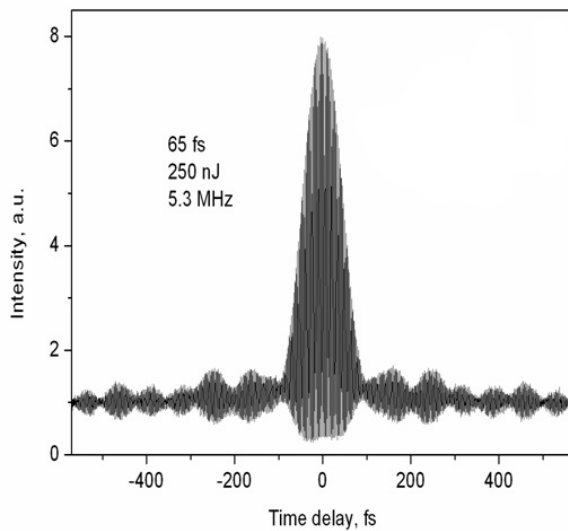


Figure 4.6: An interferometric autocorrelation trace of compressed pulses of the oscillator in a configuration with a shorter cavity.

As already stated, the laser output consists of heavily chirped long pulses, which were post-compressed by means of many reflections on highly dispersive (chirped) multilayer mirrors which were produced in-house, featuring a GDD of about -1500 to -2000 fs². Fig. 4.7 shows the very simple compressor array. The number of reflections was optimized to get the shortest possible autocorrelation signal of the laser pulses. The compressed pulse duration was about 70 fs, whereas the power losses of the beam going through the setup were below 10%.

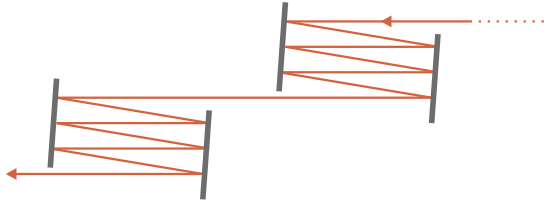


Figure 4.7: Laser pulse compression scheme: Beam coming directly out of the oscillator (upper right corner) experiences 12 bounces on chirped mirrors.

4.1.2 Higher-harmonic-generation from the laser output

An important goal of this thesis was to drive the electron gun with different light frequencies, in order to compare photoemission process efficiencies and effects on the photoelectron energy distribution. In section 4.2 it is shown that an operation of the gun with the laser fundamental had considerable disadvantages, which were overcome only by the use of higher harmonics.

As explained in section 2.4, the photon energy of the laser light, only 1.55 eV corresponding to its carrier wavelength of 800 nm, was much too low for a first-order photoelectric effect — to surpass the expected cathode work function, about three times this energy was necessary. Therefore, the second and third harmonic of the fundamental light frequency was generated by means of conventional techniques: second-harmonic generation (SHG) and sum frequency generation (SFG) by nonlinear phenomena in birefringent crystals. SHG doubles the frequency, whereas the summation of fundamental and doubled frequency in a SFG process results in laser light with tripled frequency.

What follows is a short excursion into nonlinear optics, to explain the higher-harmonic-generation processes, see [30, 31, 32] for references. Firstly, for ordinary light intensities (what the human eye is used to, e.g. daylight), the response of a medium to the light's electric field \mathbf{E} is linear, i.e. the macroscopic polarization \mathbf{P} is given by

$$\mathbf{P}(t) = \varepsilon_0 \boldsymbol{\chi}^{(1)} \mathbf{E}(t) \quad (4.2)$$

where ε_0 is the electric permittivity and $\boldsymbol{\chi}^{(1)}$ is the first-order electric susceptibility. Both electric field and polarization are vector quantities, and the susceptibility is a second rank tensor. Written in individual vector components, the above equation looks like this:

$$P_i(t) = \varepsilon_0 \sum_j \chi_{ij}^{(1)} E_j(t) \quad (4.3)$$

In general, there are higher-order contributions to the full polarization \mathbf{P} :

$$P_i(t) = P_i^L(t) + P_i^{NL}(t) = \varepsilon_0 \sum_j \chi_{ij}^{(1)} E_j(t) + \varepsilon_0 \sum_j \sum_k \chi_{ijk}^{(2)} E_j(t) E_k(t) + \dots \quad (4.4)$$

where superscript L stands for linear and NL for nonlinear portions. The susceptibility of order n is a tensor of rank $n + 1$. For sufficiently high light intensities, which means sufficiently strong electric field amplitudes, the response of a medium to the light's electric field is not linear anymore, and the nonlinear polarizations do play a role. One can show that the wave equation inside the medium then takes the form

$$\nabla^2 \mathbf{E}(\mathbf{r}, t) - \frac{n^2}{c^2} \frac{\partial^2 \mathbf{E}(\mathbf{r}, t)}{\partial t^2} = \mu_0 \frac{\partial^2 P^{NL}(\mathbf{r}, t)}{\partial t^2} \quad (4.5)$$

The nonlinear polarization acts as a source term for the wave equation, which means that it adds new partial waves to the spectrum. Inserting the spectral decomposition of the electric field

$$E_i(t) = \int d\omega E_i(\omega) e^{-i\omega t} \quad (4.6)$$

into eq. (4.4) and considering that the susceptibilities may also depend on the frequencies, the second-order polarization is obtained as

$$P_i^{NL}(t) = \varepsilon_0 \sum_j \sum_k \int d\omega_m \int d\omega_n \chi_{ijk}^{(2)}(\omega_m, \omega_n) E_j(\omega_m) E_k(\omega_n) e^{-i(\omega_m + \omega_n)t} \quad (4.7)$$

Obviously the time dependence of this polarization contains the sums of the field's frequencies. So the nonlinear polarizations drive additional electromagnetic fields whose frequencies are sums of the original frequencies. This is the principle of SFG. For SHG, which is just a special case of this general principle, the two fields $E_j(\omega_m)$ and $E_k(\omega_n)$ are identical, they can both be named $E_j(\omega)$, and the frequency sum is just the doubled frequency, 2ω .

One should note that SFG according to this scheme is only possible if the respective components of χ of the medium are nonzero — this is only the case for non-centrosymmetric crystals, i.e. crystals without inversion symmetry in their structure. For all other materials, the second-order susceptibility vanishes, which means that there are only odd orders (third, fifth, etc.) in the nonlinear polarization. So for SFG, one needs special crystal materials of the non-centrosymmetric type.

There are still some more peculiarities to higher-harmonic generation. The dipole radiation that could in principle be emitted by the nonlinear polarization contributions must also be able to propagate in the medium. Every medium has a dispersion relation defining $k(\omega)$ (wavenumber dependence on frequency) which has to be fulfilled in order for any excitation to propagate. The problem is demonstrated in a simple example based on the above formulas: Consider a fundamental radiation polarized in x direction, propagating along the z axis through a medium suitable for SFG, containing only one single frequency ω_1 .

$$E_x(z, t) = A e^{i(k_1 z - \omega_1 t)} \quad , \quad (4.8)$$

where $k_1 := k(\omega_1)$ and A is an amplitude high enough for the nonlinear processes to become effective. Note that the spatial dependence, which was hidden inside the complex fields in eq. (4.6), is now written explicitly. The radiation drives nonlinear polarizations of the medium (not necessarily along the same axis as the radiation polarization itself):

$$P_i^{NL} = \varepsilon_0 \chi_{ixx}^{(2)}(\omega_1, \omega_1) E_x^2(z, t) = \varepsilon_0 \chi_{ixx}^{(2)}(\omega_1, \omega_1) A^2 e^{i(2k_1 z - 2\omega_1 t)} \quad (4.9)$$

It is obvious that this oscillating polarization radiates a field with frequency $\omega_2 := 2\omega_1$ and a wavenumber $k_2 := 2k_1$. But this second-harmonic radiation can only propagate efficiently in the medium (and coupled out of it) if the condition

$$\Delta k = k_2 - k(\omega_2) = 0 \quad (4.10)$$

is fulfilled, i.e. the new wavenumber satisfies the dispersion relation. In that case, one speaks of phase-matching. Using $k(\omega) = \omega n(\omega)/c$ with refractive index n , the condition may as well be expressed as $n(\omega_1) = n(\omega_2)$. But for any usual material with normal dispersion, this is never fulfilled in the first place, there is always a phase velocity mismatch between different radiation frequencies, and they interfere destructively for the most part.

Nevertheless, there are several possibilities to achieve phase matching. The most prominent method which was also used in this thesis is angle tuning in a birefringent crystal, which exploits the fact that the refractive index is dependent on the light's polarization and its propagation direction. If the polarizations of fundamental and second harmonic are different and the crystal is correctly oriented, the refractive indices for ω_1 and $2\omega_1 = \omega_2$ can be made equal.

The simplest birefringent crystals are uniaxial, which means they have one distinguished axis called the optical axis. The propagation direction (which is the direction of the vector \mathbf{k}) and the optical axis enclose an angle θ , and both directions define a plane (which contains both the optical axis and \mathbf{k}). Now a light polarization *perpendicular* to this plane is called *ordinary* polarization and experiences the ordinary refractive index n_o . A polarization *in* the plane (perpendicular to the ordinary) is the extraordinary polarization and follows the extraordinary refractive index n_e (see fig. 4.8). The latter is furthermore dependent on the angle θ according to

$$n_e^2(\theta) = \left(\frac{\sin^2 \theta}{\bar{n}_e^2} + \frac{\cos^2 \theta}{n_o^2} \right)^{-1} \quad (4.11)$$

where \bar{n}_e is the so-called principal value of the extraordinary index ($n_e(\theta = 0) = n_o$ and $n_e(\theta = 90^\circ) = \bar{n}_e$). The crystal can be negative uniaxial ($\bar{n}_e < n_o$) or positive uniaxial ($\bar{n}_e > n_o$). Furthermore, it is distinguished between type-1 phase-matching, where both (or the one single) incident frequencies are polarized in the same direction, and type-2 phase-matching, where they are perpendicular.

For the above example and the case of a negative uniaxial crystal, one could find phase-matching via

$$n_e(2\omega_1, \theta) = n_o(\omega_1) \quad (4.12)$$

for a certain angle θ . Note that the phase-matching condition is that simple only for SHG — in the general case of mixing two different frequencies ω_1, ω_2 to obtain their sum ω_3 , the condition in terms of refractive indices takes the form

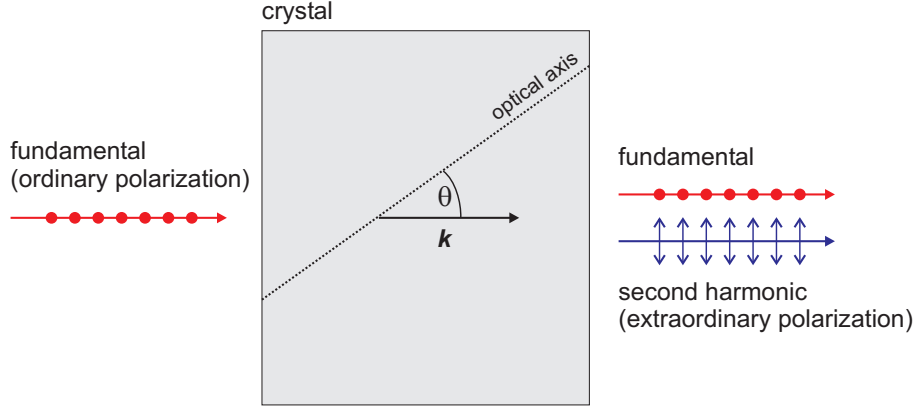


Figure 4.8: Illustration of phase-matching by exploiting the birefringence of a crystal. Propagation vector \mathbf{k} and the crystal's optical axis span a plane; light with perpendicular (ordinary) polarization with respect to that plane is subject to a different dispersion relation than light with parallel (extraordinary) polarization. Shown is an example for type-1 SHG, where the fundamental radiation is ordinarily, the resulting second harmonic extraordinarily polarized.

$$\omega_3 n(\omega_3) = \omega_1 n(\omega_1) + \omega_2 n(\omega_2) \quad (4.13)$$

To fulfill this constraint, it may become necessary to make use of type-2 phase-matching.

In addition to phase-matching, the problem of group velocity mismatch (GVM) has to be considered. Due to group velocity dispersion, light pulses with different carrier frequencies travel through the medium at different speeds. And usually it is impossible to compensate for phase velocity mismatch and GVD at the same time. In practice, the GVM leads to an increase in pulse length for the higher harmonic pulse; it can grow much longer than the fundamental laser pulse. To stick to the above example of an SHG process: Consider a pulse with the fundamental frequency ω_1 as its carrier entering the SFG crystal medium, moving with group velocity v_{g1} along the z axis. Inside the temporal window of the pulse duration, the ω_2 pulse builds up all the time (as long as the fundamental mode is not too weak). But this ω_2 pulse moves (assuming normal dispersion) slower than the fundamental, with v_{g2} . For each of both pulse centers, the time related to the distance z it has covered is $t(z) = z/v_g$. The second harmonic pulse falls behind and there is an increasing temporal distance between the two pulses, called temporal walk-off:

$$\Delta t(z) = z \left(\frac{1}{v_{g2}} - \frac{1}{v_{g1}} \right) \quad (4.14)$$

When the walk-off reaches the duration τ_1 of the fundamental pulse and grows even further, the second harmonic pulse becomes longer than τ_1 , which is not wanted in most applications where ultrashort pulses are required. So to avoid this, one has to

limit the interaction length of the fundamental and higher-harmonic radiation, i.e. the length of the crystal L , to [33]

$$L_{max} \approx \frac{\tau_1}{v_{g2}^{-1} - v_{g1}^{-1}} \quad (4.15)$$

On the other hand, the longer the path (or the propagation time) through the nonlinear medium, the more energy is transferred into the higher-harmonic radiation, even if it is distributed over a quite long pulse length, so the conversion efficiency increases with L . There is a trade-off between the shortness of the higher-harmonic pulse and the higher-harmonic pulse energy.

The crystal length L plays still another role in the issue. The spectral bandwidth of a nonlinear crystal for efficient SHG decreases with increasing L , so a long crystal cannot support the broad spectrum of an ultrashort laser pulse. As a result, the conversion efficiency can even be decreased significantly for crystals which are too long. For transform-limited pulses, the constraint on L due to this effect is in agreement with the constraint imposed by GVM as it is outlined above, demanding that $L \leq L_{max}$ [31].

In the experiments, first a frequency-doubling stage was incorporated into the laser beam line, which converted the infrared light with 800 nm center wavelength to 400 nm blue light, and later a setup for third-harmonic generation was built, which converted the fundamental into UV light with 266 nm wavelength.

For the SHG two different beta barium borate crystals (β -BaB₂O₄, abbreviated BBO) from the Lithuanian supplier EKSPLA were used with thicknesses of 0.3 mm and 0.5 mm. These values exceed the L_{max} recommended by Ekspla's datasheets for our parameters, which was about 0.2 mm. In a first stage, the shortness of the pulses was not that critical (as the RF cavity for ultrashort electron pulse generation was not available anyway), but we wanted to make sure that the higher-harmonic laser power is sufficient, so we decided for somewhat larger crystal lengths or thicknesses. The crystals' cut angle θ (identical to the above-mentioned θ) was 29.2°. The laser fundamental was focused by lenses with focal length f of either 175 mm or 75 mm into the crystal (depending on how much efficiency was needed) and recollimated behind the crystal. Assuming a laser pulse duration of 70 fs, one can estimate the peak intensity in the focus for $f = 75$ mm to $3 \cdot 10^{11}$ W/cm² (in consideration of the M^2 -value of 1.3) [29, 34]. In this configuration, from about 1.0 W average laser power in the fundamental, more than 40 mW of power in the doubled frequency were achieved, corresponding to a conversion efficiency of over 4%.

The third-harmonic generation (THG) was not as straightforward as the SHG, because there are some complications for the sum frequency generation: Firstly, for an ideally oriented SHG crystal, the 400 nm light is polarized perpendicular to the fundamental, which renders a type-1 SFG process impossible. Secondly, the GVM has already led to a weak temporal overlap between 800 nm and 400 nm pulse, as well as to a broadening of the latter, reducing its peak intensity — and especially for our case where relatively little 400 nm power was available, every bit of intensity was critical to produce enough UV light. Usually, both problems are overcome by inserting a special $\lambda/2$ -plate (which decreases the relative polarization angle) and a retardation plate (for GVM compen-

sation) *between* the SHG and SFG crystal — this is relatively easy if one works with a common kHz laser system producing ultrashort pulses with energies of hundreds of microjoules or more, because then it is not absolutely necessary to focus the beam, its peak intensity already being high enough. But in our case, we had to focus and could not afford to make the focus long enough to be able to place all those optical elements in the focus. On the other hand, *refocusing* into the second crystal was also not a good option, because then the temporal walk-off and the second-harmonic pulse broadening would have been quite large.

So it was first tried to generate the third harmonic via surface-enhanced *direct* THG, where the frequency-tripling mechanism via the third-order susceptibility of the material is used and an enhancement effect occurring at interfaces due to the interplay between group and phase velocity mismatch is exploited [35]. The fundamental beam was focused on the surfaces of UV-transparent substrates with a variety of different coatings, from single-layer Ta₂O₅ and TiO₂ to multi-layer dielectric mirrors. Indeed a THG effect was found, but for all samples it was very weak — the average UV powers achieved lay all below 100 nW, corresponding to a conversion efficiency below 10⁻⁷.

It was found that, despite the problems mentioned before, the far more effective option to generate 266 nm light pulses was the SFG, in a scheme where the SHG crystal and the SFG crystal were placed close to each other in one and the same laser focus, with no additional optics in between, but with a significant rotational detuning of the SHG crystal in the ϕ coordinate: The polarization of the 800 nm light was not perpendicular to the plane defined by \mathbf{k} vector and the crystal's optical axis, but in an angle of around 45°, which means that a part of it (the perpendicular component) could drive the SHG, whereas the remaining component (polarized in the same direction as the 400 nm light) was used in the type-1 SFG process where 800 nm and 400 nm light combined to 266 nm radiation, see fig. 4.9. For the SFG combining the 800 nm and 400 nm light, a BBO crystal with thickness 0.3 mm and cut angle $\theta = 44.3^\circ$ was used. It was situated 10 mm behind the SHG crystal (a smaller distance was impossible due to mounting rings), and the UV power was at a maximum when the laser focus was located in the middle of those 10 mm free space between the crystals. A time-averaged UV output of 500 μ W was achieved, i.e. conversion from 800 nm to 266 nm was possible with an efficiency of $5 \cdot 10^{-4}$.

It is important to note that the UV power was strongly dependent on the width of the oscillator's spectrum, which had to be optimized by adjustment of the prism pair inside the laser cavity. To obtain 500 μ W, the fundamental spectrum had to be broader than 40 nm, around 45 nm at least, and a decrease in spectral width by a few nm could result in a UV power drop-off by a factor of 5 or more. For reliable UV generation, the oscillator spectrum had to be quite stable — in practice, a UV power output with $\pm 50\%$ stability could be maintained for about one hour.

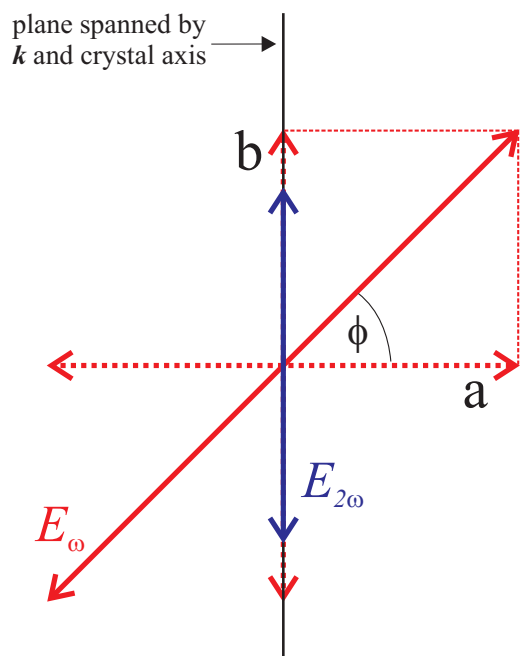


Figure 4.9: Illustration of the light polarizations in the combined SHG-SFG-process to generate the third harmonic of the laser output: The black vertical line indicates the plane spanned by propagation vector (pointing into the drawing plane) and crystal axis. Due to angular detuning of the SHG crystal in ϕ , the fundamental's polarization (red) is at around 45° with respect to that plane. Its ordinary component (a) provides for the generation of the second harmonic (blue) in type-1 manner, whereas its remaining extraordinary component (b), parallel to the 400 nm polarization, enables the type-1 SFG of infrared and blue light to UV (third-harmonic) radiation.

4.1.3 The electron gun

The scheme of a photoemission-based electron gun has already been described in section 2.1. A drawing of our specific electron gun is shown in 4.11. The laser beam could be focused by lenses outside the vacuum chamber onto the photocathode in either normal or slightly oblique incidence; the latter option was used to avoid pointing the laser beam (at least the transmitted fraction of it) directly onto the detector. The photocathode consisted of a fused silica disk (1 mm thickness) coated with a thin metal film (gold or copper) on the side facing the anode. The film thickness was usually 50 nm and it was deposited on the silica by vacuum deposition at 10^{-7} mbar. By heating, the metal was evaporated onto the substrate and, at the same time, onto an oscillating crystal whose frequency changed with the amount of deposited metal, providing a means of controlling the metal layer thickness. In the electron gun, the coated silica disk was clamped in a specially designed holder and the metal film was in contact with a high-voltage supply through a thin metal ring pressed on the edges of the coated surface (see fig. 4.10). As it would have been difficult to isolate the metal film and metal ring against the other parts of the holder, and charging of an isolating material was to be prevented, it was decided simply to make the whole holder out of metal (brass) and isolate the complete holder against the surrounding vacuum chamber by mounting it on a high pedestal made of acrylic glass.

There were two different types of anodes available:

1. A simple copper cylinder with a hole of 1 mm diameter and 1 cm length
2. A metal wire grid (2 cm diameter) in a circular frame, with a mesh size of $83 \mu\text{m}$

The vacuum chamber was composed of an in-house standard system of chamber parts made of anodized aluminum. The main elements were hollow cubes (edge length 20 cm) with circular openings on each side, which could be closed by different types of flanges. Special flanges could be mounted which e.g. contained a transparent window or had the form of drift tubes, by which two of the cubes could be connected. For the vacuum sealing, conventional rubber o-rings were used. A high-voltage (HV) feedthrough provided electrical contact of the external HV supply (max. 30 kV) to the negative-potential wire inside the chamber, to which the cathode was connected. The combination of a pre-pump (Vacuubrand *MD4T*) for pressures down to 2 mbar and a turbo pump (Pfeiffer *TPU 180 H*) with a volume flow rate up to 180 l/s reduced the pressure in the chamber to a few 10^{-5} mbar. Even if the chamber had been open for days, such a pressure was usually achieved in about 1.5 hours, and for all experiments, the pressure was always below 10^{-4} mbar. The vacuum diagnostics were a Pirani gauge (Thermovac sensor) and a Penning gauge from Leybold-Heraeus. Figs. 4.12, 4.13 and 4.14 show photographs of the setup.

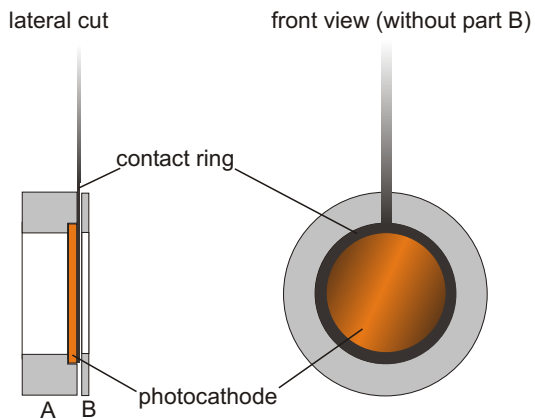


Figure 4.10: The cathode holder, consisting of two parts A and B, made of brass (gray). B is fixed on A by screws (not shown), pressing the metallic contact ring against the coated surface of the cathode disk.

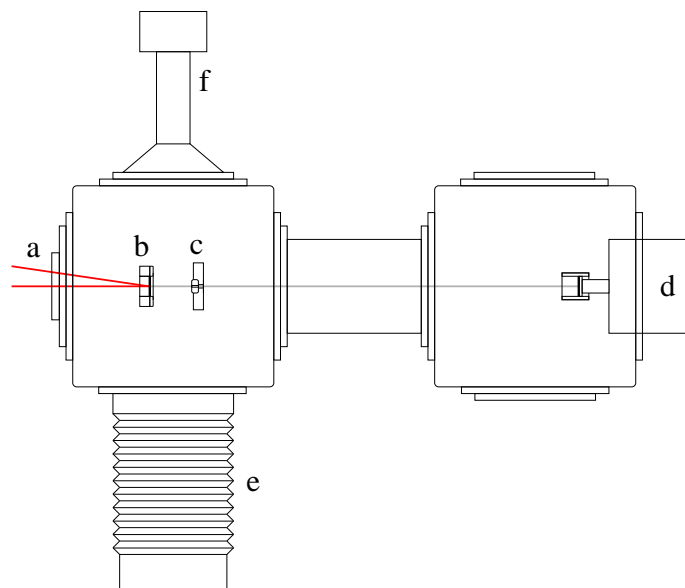


Figure 4.11: Drawing of the electron gun, top view (proportions not exact): (a) laser entrance window, (b) cathode, (c) anode, (d) detector, (e) turbo pump, (f) vacuum diagnostics. The two red lines indicate the two possible laser beam orientations (normal or oblique incidence on cathode), the gray line indicates the electron beam. The high-voltage feedthrough is on the top side of the left cube and therefore not illustrated here.

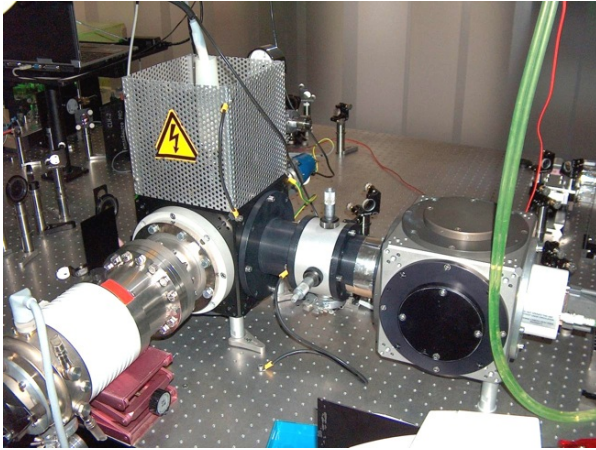


Figure 4.12: The electron gun, here set up with an extended electron beam line, lengthened by a target chamber (gray, with the two actuators) and an additional tube part. The white cylinder to the very right is the CCD camera.

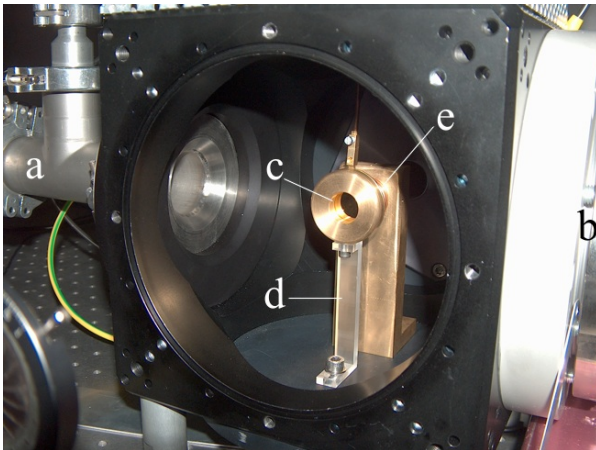


Figure 4.13: View into the opened acceleration stage, from the side where the laser enters the chamber. To the left, there are the vacuum diagnostics (a). The connecting flange of the turbo pump is on the right (b). Inside, one can see the cathode in its brass holder (c), mounted on a stand of acrylic glass (d), and a small part of the anode is visible behind (e).

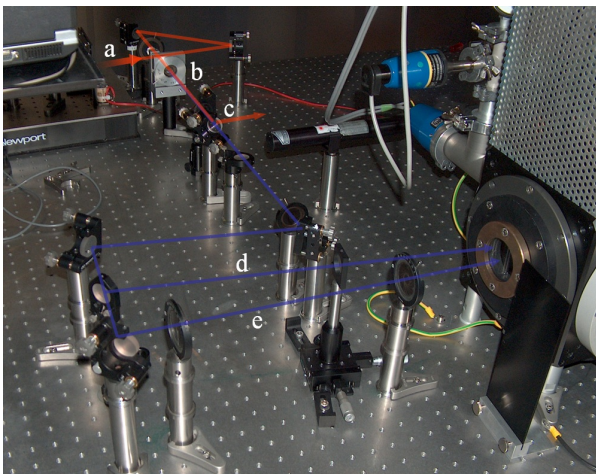


Figure 4.14: The laser beamline as it was configured for second-harmonic generation (beams indicated by colored lines): The infrared beam (a) coming from oscillator and compressor (not visible here) is focused into the BBO crystal (b), second harmonic and fundamental are separated by a mirror which is highly reflective for 800 nm (c), the beam is then directed through a window onto the cathode in oblique (d) or normal incidence (e).

The detector system is illustrated in fig. 4.15. The screen which was hit by the electrons was a layer of scintillating material ($P43$ phosphor screen from Proxitronic), i.e. it responded to the impact of each electron by emission of several hundred photons with wavelengths around 545 nm *at* the exact location of the electron's impact. The very thin $P43$ screen covered almost the whole surface of a fiber plate with diameter 37 mm and was itself covered by a protective aluminum coating with about 100 nm thickness, reducing unwanted background light by orders of magnitude while admitting the electrons. The fiber plate and the fiber taper on which the plate rested captured the spatial distribution of light signals from the screen and imaged this data directly onto a CCD (charge-coupled device). The CCD camera was a *CH350* from Photometrics, cooled by a Peltier element to temperatures of -25 to -30 °C to reduce thermal signal noise. The heat produced by the Peltier cooling unit was led off by a continuously running water circuit. The CCD chip itself was a SITE model *003B* with a resolution of 1024x1024 pixel, and a pixel size of 24 micron. Its quantum efficiency was 60–80% for light in the wavelength range emitted by the scintillator.

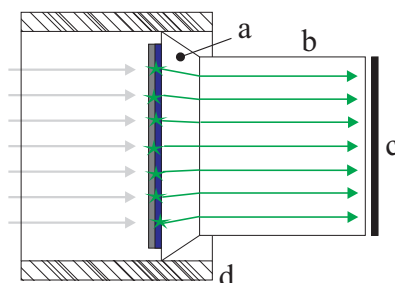


Figure 4.15: Scheme of the electron detector: Incident electrons (gray arrows) pass an aluminum layer (dark gray) and hit an underlying scintillator screen, leading to short-lived local excitations in the material which decay via isotropic emission of photons (green), a part of which are then guided through a fiber plate (a) and a fiber taper (b) onto a CCD (c), where the optical signals are converted into electronic signals for digital processing. The coated circular fiber plate is surrounded by a black metal cylinder (d) which blocks stray light from the sides.

The digital image from the CCD was read out and processed by the software *PMIS* (from Photometrics) on a usual PC. The images could be stored as 16-bit grayscale bitmaps in TIFF (tagged image file format) files. In such a bitmap, every pixel contains only one value (the grayscale value) which, in this case, corresponds to the number of signal counts in the respective physical pixel of the CCD chip. The 16-bit resolution allows for values either from 0 to 65535 (only positive numbers) or from -32768 up to 32767 (one bit storing the sign). Our device worked in the latter mode, supporting the effective 15-bit dynamic range of meaningful count values from 0 to 32767. The counts were collected during an integration period set in the software, which could in principle range from single milliseconds to many hours. By contrast, the read-out process loading the data from the CCD chip into the computer's memory took about 5 s if the whole CCD area was active. This time could be reduced to fractions of a second by defining just a small region of interest (ROI) out of the whole 1024x1024 pixel area before the acquisition was started. If a CCD pixel received too much signal during integration, its counter could overflow and continue to count up from -32768,

resulting in negative count values which make no sense and render the CCD image useless for quantitative analysis. Therefore, a too strong signal on the detector had to be avoided. A great advantage of the digital image acquisition are the rich options of post-processing: It was often important to subtract the unwanted background from the electron beam image. This could be done simply by repeating the acquisition under the same conditions, only without the electron beam (i.e. with the HV supply switched off) and subtracting this image from the one with the electron beam signal. Apart from a more or less constant background (e.g. from stray light), there was always a small amount of random noise, and a subtraction of two images with random noise can lead to negative count values in some pixels. For this reason, after such an image subtraction, a command was used to restrict the allowed pixel values to positive numbers, setting all counts below zero to zero. With this subtraction technique, even a very weak electron beam could be made visible.

4.2 Results and discussion

4.2.1 Electron yield from the cathode

For our purposes it is important to know a relation between laser intensity incident on the cathode and resulting electron yield — since a reproducible beam current is necessary to produce single-electron pulses. Especially for the higher-order photoemission it was unclear from the beginning if the efficiency for such a process was high enough to release enough electrons from the cathode metal with the available laser power. For the pulse repetition rate f , the expected electron current is easily estimated to be around

$$f \cdot e = 2.8 \cdot 10^6 \text{ Hz} \cdot 1.6 \cdot 10^{-19} \text{ C} = 0.4 \text{ pA}$$

The beam current could be inferred from the total intensity of the beam profile images received at the detector. The co-group at the Max-Planck-Institute of Quantum Optics (MPQ), consisting of P. Reckenthäler and M. Centurion, had found their detector response, i.e. the number of counts produced by the CCD *per* incident electron:

$$\eta = 7.1 \pm 0.6 \text{ counts/electron}$$

This calibration was done by comparison of the counts the CCD detector registered for the electron beam with the beam current measured directly with a Faraday cup (model *FC-70C*, Kimball Physics) and a picoammeter (model *480*, Keithley). The same η value was assumed for the detector used here, for it was completely equal to the model used by the MPQ group (including the fiber plate and its coatings). An attempt was made to do our own calibration, but the beam currents in our electron gun were too low to make a meaningful measurement, since they were at the resolution limit of the picoammeter (1 pA).

With this information at hand, the total count number inside an electron beam spot in the CCD image could be obtained by integrating the pixel values, and a division by η revealed the number of electrons that had hit the detector in this region. Of course, the background signal was subtracted beforehand, according to the procedure described in section 4.1.3. By normalizing the number of electrons with respect to the integration time, the electron rate or the beam current was obtained.

Cathode irradiation with fundamental, second and third harmonic light

The cathode used in all measurements presented in this subsection was the most commonly used cathode with a 50 nm thick gold layer.

It turned out that even with our laser fundamental it was easily possible to achieve a sufficiently high electron yield. The laser beam was attenuated to a few hundred mW of average power and focused with a focal length $f = 300$ mm. The highest laser power ever used to illuminate the cathode was 650 mW (230 nJ pulse energy), which resulted in a focal peak intensity of about $3 \cdot 10^{10} \text{ W/cm}^2$, releasing $5 \cdot 10^6$ electrons per second. This corresponds to a beam current of 0.8 pA, or two electrons per pulse. Unfortunately, the efficiency of the photoelectric effect was not very reproducible. It

varied with the exact location on the cathode where it was hit by the laser; there were “hot spots” where the electron yield suddenly rose by more than an order of magnitude. Additionally there was a considerable degradation of the yield over time if one and the same spot on the cathode was irradiated for more than a few seconds. During minutes, the yield could decrease by an order of magnitude. This behavior is presumed to be caused by microscopic surface roughness features, probably leading to those hot spots, and adsorbates on the metal like oxygen or water remnants, which could enhance the photoemission efficiency during the first seconds and then slowly evaporate due to thermal effects of the high laser intensity. Similar effects with high laser intensities on photocathodes have been observed before [36] under very similar vacuum conditions. Visible damages to the thin metal layer due to laser irradiation were not found under the microscope.

To clarify which kind of photoemission dominated here (third or even higher order), a measurement of the correlation between incident laser intensity and electron yield was done. Of course, this measurement was hindered by the problem described above. The values shown in fig. 4.16 are results of a measurement where the photoemission efficiency seemed to remain more or less constant. Every value is the result of three shots (image acquisitions), the vertical error bars are the standard deviations from the mean values, whereas the horizontal error bars indicate the fluctuations in laser power.

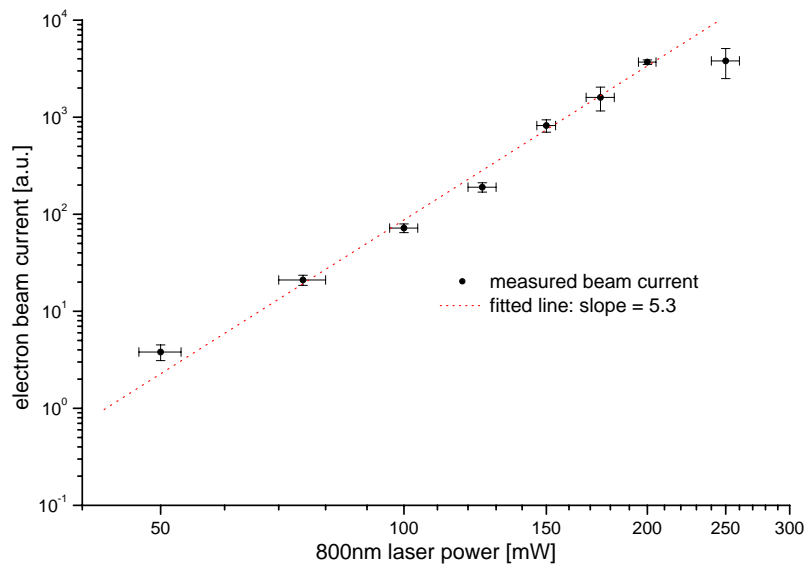


Figure 4.16: Correlation between 800 nm average laser power (constant beam focusing) and electron yield from the gold cathode, shown in a double-logarithmic plot. The slope of the fitted line indicates the polynomial order of the dependence.

The slope of the fitted line reveals that there is approximately a fifth order correlation between electron yield and laser power, which means that not the third, but even the fifth order photoemission is dominant, which is for sure an ATP process, because five photons have a combined energy of $5 \cdot 1.55 \text{ eV} = 7.75 \text{ eV}$, and this is certainly far above the work function of the metal film which should be around 4 eV (see p. 20).

For the second harmonic (400 nm wavelength) of the laser, each photon carries an energy of 3.1 eV, and since two such photons in combination exceed by far the assumed work function, a second-order photoemission process was expected. Indeed, this was found to be the case, as one can see in fig. 4.17.

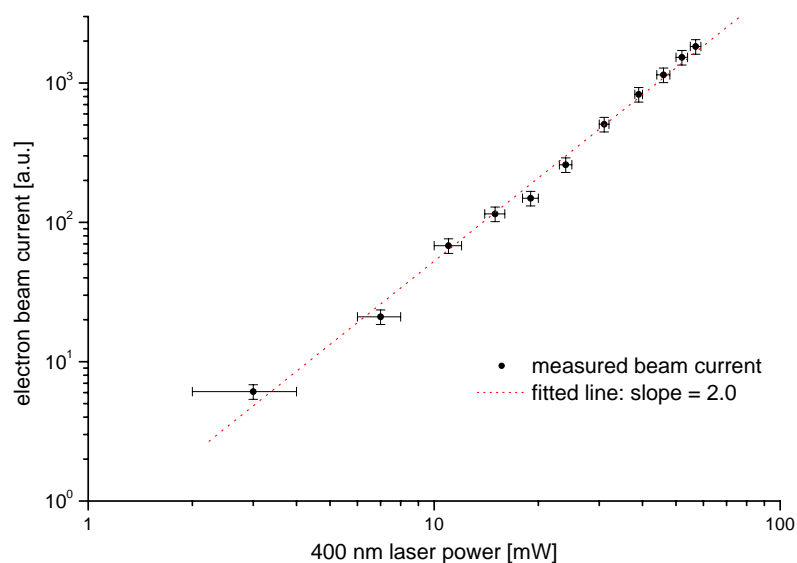


Figure 4.17: Correlation between 400 nm average laser power and electron yield. The line with a slope of 2.0 matches the measured data points quite well, indicating a pure second-order dependence.

Only low power of second harmonic light was needed to achieve about the same or even higher electron yield than with the fundamental: A few nJ of laser pulse energy were sufficient, a fact which confirms the expected higher efficiency for a lower-order photoelectric effect. The focusing optics were the same as in the case of 800 nm.

Obviously, the efficiency for a first-order process is still orders of magnitude higher. The third harmonic with about 266 nm wavelength provides a single-photon energy of 4.65 eV, which was assumed to lie above the cathode's work function, so a direct linear photoemission was expected. This was well confirmed by the measurements, as shown in fig. 4.18. In combination with the result from the 400 nm photoemission, one can say that the work function of the thin gold film lay definitely between 3.1 eV and 4.65 eV, in accordance with [24]. Note that this thin-film work function differs significantly from the value of 5.1 eV given in the literature for polycrystalline bulk material [37].

As already stated in section 4.1.2, an average UV light power of 500 μ W (i.e. about 20 pJ pulse energy) could be produced, and this was sufficient to reach electron yields in the same order of magnitude as with the fundamental and second harmonic light.

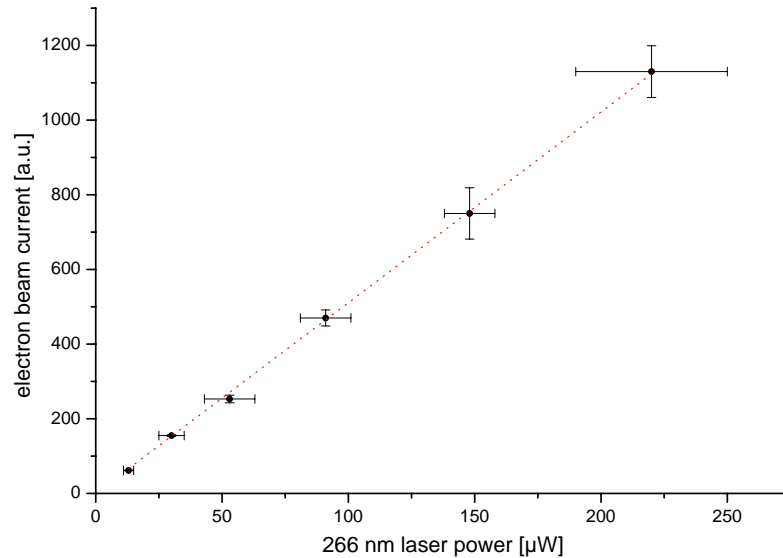


Figure 4.18: Linear correlation between 266 nm average laser power and electron yield.

To summarize, the photoemission via second and third harmonic worked quite reliable, which means that the electron yield for a given laser power was well reproducible, whereas with the laser fundamental one never knew what beam current to expect, and an adjustment of laser power and beam focusing to maximize the electron yield often helped only for a few minutes because then the performance could degrade severely. Another issue was the unpredictable dependency on the location where the cathode was illuminated, including hot spots or regions of poor efficiency which could not be assigned to visible features on the cathode's surface.

Comparison of different cathodes

Apart from gold, copper could also be deposited in thin films on the quartz substrates, so a few copper cathodes were produced for comparison. Of course, in contrast to the noble metal, copper oxidizes quite quickly when exposed to air, so the copper cathodes had to be handled more carefully to avoid oxidizing as far as possible: They were stored in an argon chamber as long as they were not used, and during transports or their installation in the electron gun, they were never exposed to air for more than a few hours.

First, the electron yields from copper and gold cathodes were compared. The result is shown in fig. 4.19: Both materials work well and deliver comparable beam currents, but the gold cathode seemed to be even slightly more efficient.

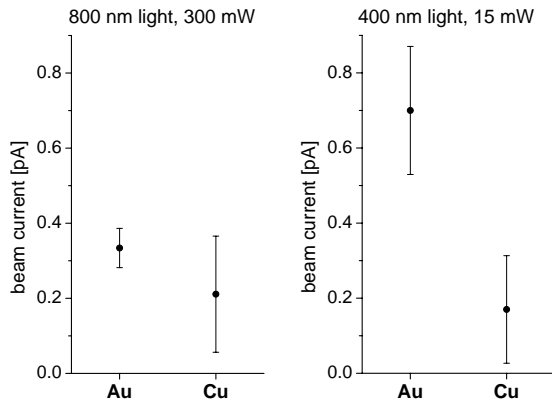


Figure 4.19: Beam currents delivered by two different cathode materials: gold (Au) and copper (Cu). A comparison was made both for 800 nm and 400 nm laser light on the cathode, in each case the laser intensity was equal for both materials.

Up to now, all the cathodes used had a metal layer thickness of about 50 nm. Now different layer thicknesses were compared, for 400 nm light on copper as an example, see fig. 4.20. From the deposition process the thickness of the metal layer could be specified with an uncertainty of $\pm 10\%$, as indicated by the horizontal error bars. The vertical error bars are again standard deviations of the beam current for several CCD image acquisitions.

It may seem surprising that the electron yield is higher for lower layer thicknesses, i.e. less material — but the thinner the film, the more light reaches the metal-vacuum-interface. In this respect it is interesting to note that in the semi-logarithmic plot the electron yield dependency on the thickness seems to follow a straight line, indicating an exponential decay of the beam current with increasing thickness of the copper film. This may possibly be attributed to the exponential damping of the light intensity in the material: If the photoelectric effect happens only at the metal surface and not in its volume, the electron yield dependence on the material thickness should be based almost only on the extinction of the light during its penetration through the material — with the modification that the electron yield has to decrease again as soon as the thickness falls below a critical value. (At least when it drops below a monolayer of atoms, the yield must obviously approach zero.)

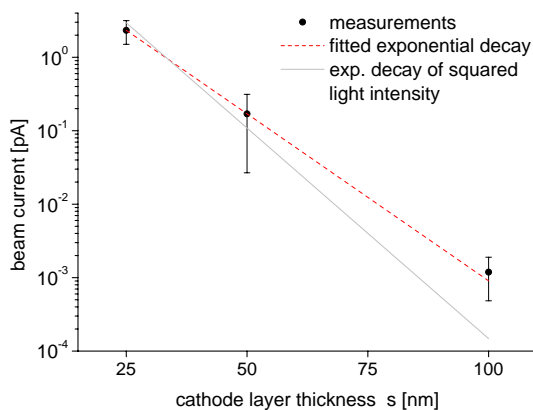


Figure 4.20: Dependency of the electron yield or beam current on the metal layer thickness of the cathode. The fitted line (red, dotted) indicates its exponential decay. For comparison, the exponential decay of the square of the light intensity transmitted through the metal layer is shown (gray).

It can be checked easily if the above assumption holds true. If the photoemission with 400 nm light is a two-photon-process, then the electron yield Y is proportional to the square of the intensity I . For light penetrating an absorbing material like a metal, the intensity falls off according to $I(z) = I(0)e^{-\alpha z}$, where α is the absorption coefficient and z is the penetration depth. If the electron yield is primarily due to

photoemission right at the cathode surface, where the laser light has already passed through a thickness s of the metal, the yield should follow a correlation like

$$Y(s) \propto I^2(s) \propto e^{-2\alpha s} \quad (4.16)$$

The fit which is shown in fig. 4.20 was done with the model $Y(s) = Ae^{-s/B}$, so $1/B$ corresponds to 2α . The fitting routine calculated $B = 9.6$ nm, so

$$\alpha = (5.2^{+1.8}_{-1.4}) \cdot 10^{-2} \text{ nm}^{-1}$$

The uncertainties are derived from the extremes in slope that a line could have within the error bars of the data points. The absorption coefficient given in the literature [38]¹, for copper and a photon energy of 3.1 eV, is $\alpha = 6.6 \cdot 10^{-2} \text{ nm}^{-1}$, specified to an accuracy of better than 10%. The exponential decay of $I^2(s)$ for this theoretical value of α is shown in the figure as well (gray). Within the uncertainties, the α value from the fit is about equal to the theoretical value expected from light extinction, which is an indication that the contribution of the volume of the irradiated metal to the electron yield is very small, if existent at all, so that only the light intensity *at* the metal-vacuum-interface plays a role, and not the total amount of material traversed on the light's way towards the interface. At least for the considered range of thicknesses, the attenuation of light is clearly the dominant effect, so the photoemission takes place primarily at the metal-vacuum interface.

The issue cannot be clarified here completely with the few data available and its high uncertainties. The goal of the cathode comparisons was rather to give a qualitative idea which cathodes are best suited regarding the aspect of electron yield. The conclusion is simply that gold films are both easier to handle and provide a slightly higher photoemission efficiency, and that the electron yield can still be increased at least by an order of magnitude by reducing the film thickness.

¹Actually not the absorption coefficient α , but the extinction coefficient k was given for photon energies of 3.0 and 3.2 eV. For a simple interpolation, the mean value of k for both photon energies was taken (2.14), and then the relation $\alpha = 4\pi k/\lambda$ was used, see also [39].

4.2.2 Electron beam profile

Similar to laser beams, a particle beam can be focused tighter and radiography or diffraction images are cleaner if the beam has a smooth symmetric transverse profile. Here a short comparison is presented how the beam profile, as seen on the detector screen, changed with the type of anode and even with the laser wavelength involved in the photoemission. Fig. 4.21 illustrates the situation with a fine-meshed grid anode (see section 4.1.3, p. 44). The acceleration distance L_a was (26 ± 1) mm, the distance from the anode to the phosphor screen was (302 ± 2) mm. The reason for the different electron beam diameters dependent on the light wavelength is attributed to differences in the initial electron energies upon photoemission, see section 4.2.3.

Interestingly, in the case of fundamental and second harmonic light, the mesh is imaged quite sharply onto the detector screen, but in the case of UV light photoemission, there is absolutely no trace of this mesh pattern. It was found that the reason is the following: The UV light was focused much weaker onto the cathode, because the UV beam was very thin (less than 1 mm in diameter), so the light spot on the cathode was relatively large. As a result, the initial electron beam diameter was equally large, wider than the mesh size of $83\ \mu\text{m}$, so the electron beam was too broad to resolve the mesh; its pattern was simply blurred out completely. In other words, due to the large emission spot diameter, the emittance of the beam was too large to deliver a sharp image of such a fine structure. A proof of this connection between focal spot size and mesh imaging could be demonstrated with the 400 nm laser beam, see fig. 4.22, and later with the 266 nm light as well.

The best way to get an electron beam which is both thin and has a clean profile without any mesh patterns, is to use the simple hole anode. Driving the electron gun with the second harmonic laser pulses resulted indeed in very nice Gaussian electron beam profiles. Driving it with the fundamental, problems arose due to the large beam divergence for high-order photoemission (as it can already be seen in fig. 4.21): The electron beam diameter grew so quickly upon photoemission that it was already larger than the hole (1 mm diameter) when it arrived at the anode. The result was a very bad beam profile which imaged the anode hole, and all its irregularities lead to strong local beam distortions with very high spatial variations of electron intensity (see fig. 4.23). Note that even in the center of the hole, where the hole's edges should not distort the beam, the intensity distribution is far from Gaussian, at least obviously worse than the high-quality profile achieved with 400 nm light. Experience showed that with the laser fundamental, the electron beam profile seldom reached the quality that it had with lower-order photoemission.

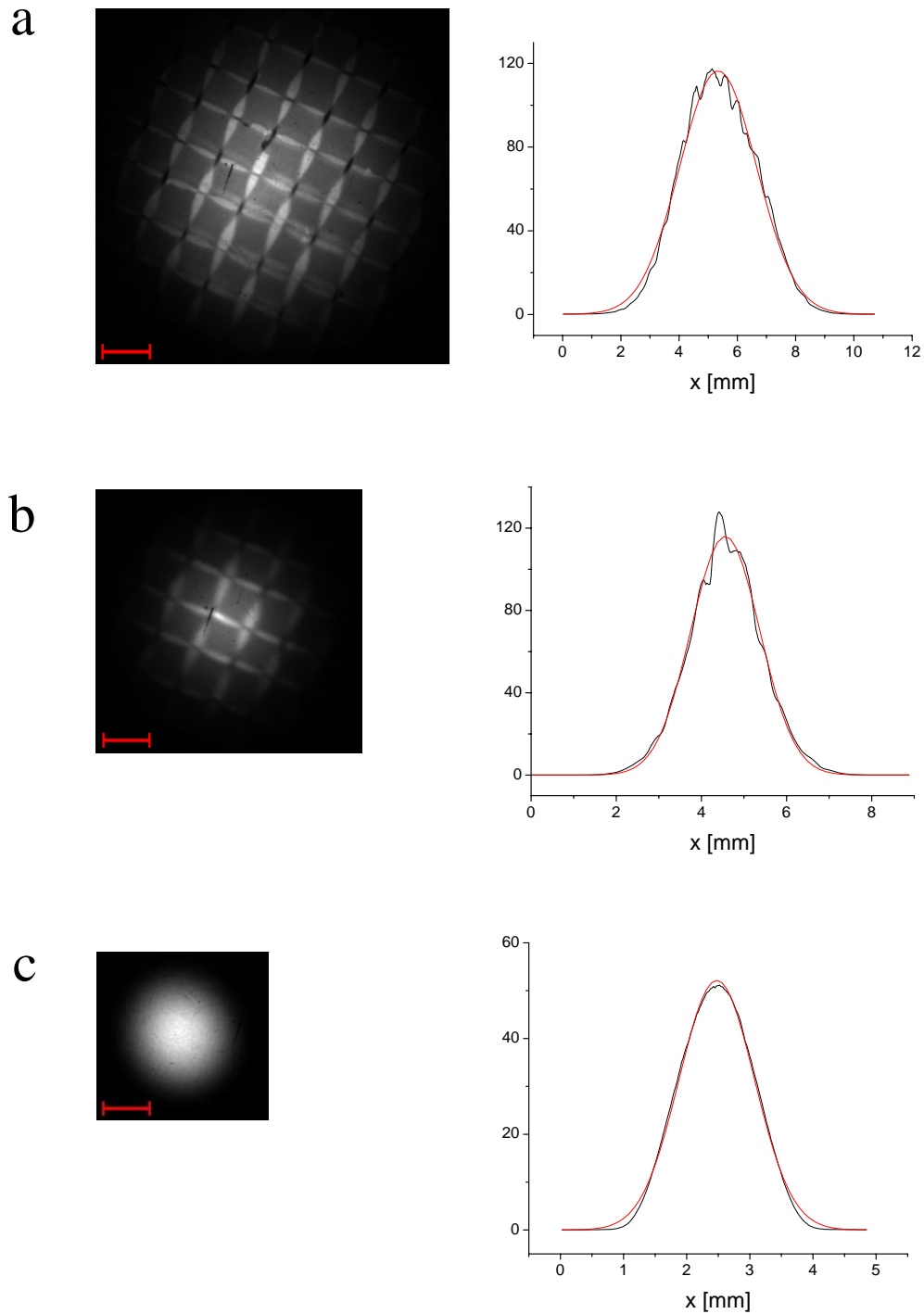


Figure 4.21: Electron beam profiles as they appear on the detector if a grid anode is installed, for the following laser light wavelengths and powers: (a) 800 nm, 510 mW; (b) 400 nm, 15 mW; (c) 266 nm, 500 μ W. On the left, the grayscale images received from the CCD are shown, where black is zero signal, white is the highest electron intensity. The red bars always indicate a length of 1 mm. On the right, 1D plots of the beam profiles are shown, obtained by integrating the respective 2D distribution along the vertical axis. The red graphs are Gauss fits on the distributions. The total distance from cathode to detector was about 328 mm, with an acceleration length of 26 mm.

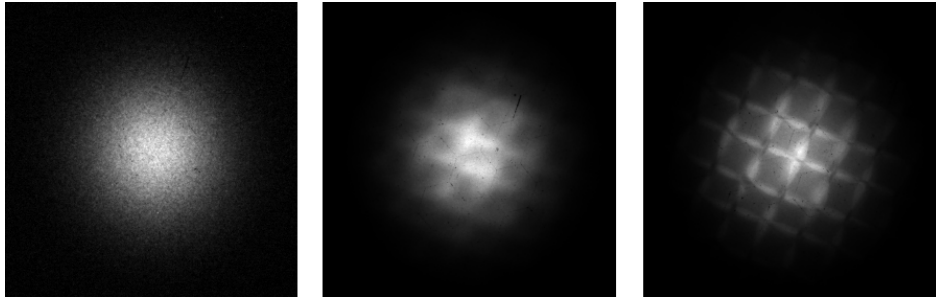


Figure 4.22: Electron beam profiles with 400 nm light incident on the cathode, under different focusing conditions (from left to right): (1) unfocused, (2) with $f = 300$ mm lens, (3) with $f = 200$ mm lens. The stronger the focusing, the smaller the laser spot size on the cathode and hence the electron beam size, and the sharper the imaging of a fine structure like the anode grid.

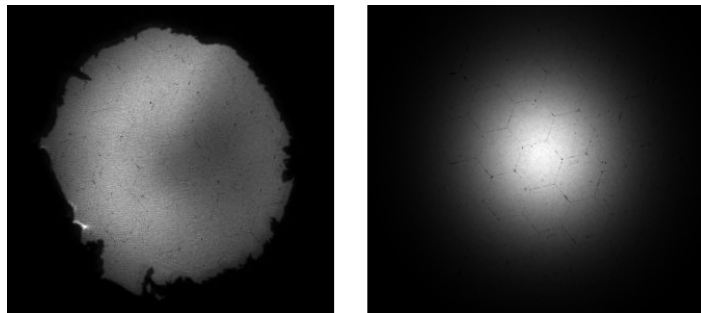


Figure 4.23: Electron beam profiles as they appear if a single-hole anode is installed, for photoemission with 800 nm (left) and 400 nm light (right). The faint hexagonal pattern which is visible on both pictures is no part of the beam profile, but is caused by the structure of the fiber plate under the phosphor screen.

4.2.3 Initial electron energy distribution

The important role of the width of the energy spread which the electrons exhibit directly upon their release into the vacuum was already pointed out in sections 2.4 and 3.3.1. Now, in our special case where space-charge effects were negligible, it was possible to get an idea of this initial energy spread experimentally, simply by analyzing the electron beam profile.

For each laser pulse, a single electron is emitted from the cathode with a longitudinal kinetic energy E_L associated with its longitudinal velocity v_L and a transverse kinetic energy E_T associated with its transverse (or radial) velocity v_T . The acceleration by the static field leads to a rapid growth only of the longitudinal velocity, whereas the transverse velocity is unaffected. After acceleration, the electron moves freely towards the detector. Its longitudinal velocity or energy is well known; at least the relative uncertainty is on the order of 10^{-4} (1 eV vs. 20 keV), so only its small transverse energy component (on the order of 1 eV or below) decides on the radial location ρ where it will hit the detector screen:

$$\rho = v_T \cdot T \tag{4.17}$$

where T is the total propagation time from the cathode to the detector. It is important to note that T itself does *not* depend on the initial velocity components, because the electrons all acquire a total energy of 20 keV and need the same time to reach the detector; a possible additional transverse velocity component (lengthening the propagation distance) can only make a relative error of 10^{-2} (square root of the energy relation E_T/E_L). Hence, the electron beam profile registered on the detector screen can be understood as a *mapping of the transverse velocity distribution* of the electrons, where a chosen radial position ρ corresponds to a certain velocity component v_T .

Assuming that the distribution of transverse velocities is known, there is still information missing about the remaining (longitudinal) dimension. To estimate the width of the total energy or velocity spectrum of the photoelectrons before acceleration, it is necessary to make an assumption about how transverse and longitudinal velocity components are correlated, i.e. about the *angular* distribution of the photoemission. The presumption of isotropic emission into the full half-sphere suggested itself for several reasons. Firstly, the metal film on the cathode was no single crystal, but a polycrystalline solid, from which one would not expect any preferred orientations of the electron velocity. Even if there were preferred directions due to some order in the material's structure, their effect would get washed out statistically by the random influence of surface roughness and adsorbates which can alter local photoemission characteristics significantly. Secondly, the results presented in section 4.2.1 indicated that the photoemission took place only at the metal-vacuum interface, so that it is not necessary to consider an increased scattering probability for photoelectrons inside the material which have a longer or shorter path through the metal depending on their initial angle with respect to the surface.

In the following, a simple but very general model is developed, describing how the photoelectron emission characteristics translate into a distribution in transverse velocity $f(v_T)$ as it is mapped onto the detector:

The probability that a photoelectron enters the vacuum with a total velocity v and in an angle θ with respect to the z axis (normal to the cathode surface) is denoted by $P(v, \theta)$. Transverse and total velocity are related by (see also fig. 4.24)

$$v_T = v \sin(\theta) \quad \text{or, equivalently} \quad \theta = \arcsin\left(\frac{v_T}{v}\right) \quad (4.18)$$

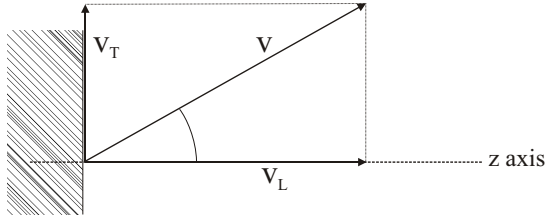


Figure 4.24: The initial velocity v of a photoelectron emitted from the cathode material (hatched area). θ is the angle to the surface normal.

Now the probability $f(v_T)$ for a photoelectron to have a given transverse velocity v_T is the integral over all possible combinations of v and θ that satisfy the constraint given by eq. (4.18):

$$f(v_T) = \int_0^{\pi/2} d\theta \int_{v_T}^{v_{max}} dv P(v, \theta) \delta(v_T - v \sin \theta) \quad (4.19)$$

where $\delta(x)$ is the Dirac delta function, and v_{max} is an upper bound of the velocity spectrum, which can in principle be chosen arbitrarily large, but finite. The lower bound of the integration over v is of course v_L , as the total velocity vector must have at least the length of its v_L component. In order to handle this expression, one has to apply the following general rule: For a delta function *dependent* on another function $g(x)$ with n roots x_i and $g'(x_i) \neq 0$ for all $i = 1, 2, \dots, n$:

$$\delta(g(x)) = \sum_{i=1}^n \frac{1}{|g'(x_i)|} \delta(x - x_i) \quad (4.20)$$

In our case we understand the argument of the delta function as a function of θ , its derivative is $-v \cos \theta$ and its only root is given by relation (4.18). Applying the above rule leads to

$$\begin{aligned} f(v_T) &= \int_0^{\pi/2} d\theta \int_{v_T}^{v_{max}} dv P(v, \theta) \frac{1}{v \cos(\arcsin(v_T/v))} \delta(\theta - \arcsin(v_T/v)) \\ &= \int_{v_T}^{v_{max}} dv \frac{P(v, \arcsin(v_T/v))}{v \cos(\arcsin(v_T/v))} \end{aligned} \quad (4.21)$$

Up to this point, the formula is valid generally. To proceed, we have to make the following assumptions. Firstly, the total velocity is not correlated with the angle of emission, i.e. $P(v, \theta)$ separates into $P_v(v) \cdot P_\theta(\theta)$. Secondly, assuming isotropic emission, P_θ is constant for all angles θ , and it can be set equal to a constant C . $P_v(v)$ is the velocity spectrum of the photoelectrons, closely associated with the initial energy spectrum, which we want to learn about. Hence, eq. (4.21) simplifies further to

$$f(v_T) = C \int_{v_T}^{v_{max}} dv \frac{P_v(v)}{v \cos(\arcsin(v_T/v))} \quad (4.22)$$

Now a third assumption has to be made on the shape and the width of the spectrum $P_v(v)$, and the resulting distributions $f(v_T)$ are compared to those observed in the experiment via the beam profile — in this manner, an energy spectrum can be fitted to the experimental data, hence giving an idea of a possible energy spectrum that one can assume to be existent in the electron gun before the electrons get accelerated. The fitted spectrum is certainly no one-to-one result, because a spectrum with a completely different shape and an accordingly different width may result in a very similar $f(v_T)$ distribution, but there are not many sensible assumptions for the spectral shape, and at least for an estimation of the energy spread this method should be helpful enough.

There remains one point to clarify, namely how a transverse velocity v_T maps to a radial coordinate ρ on the detector. The z axis of the cylindrical coordinate system is again defined as the beam axis. Fig. 4.25 shows an electron trajectory in space, seen as if one looked onto the beam from the side.

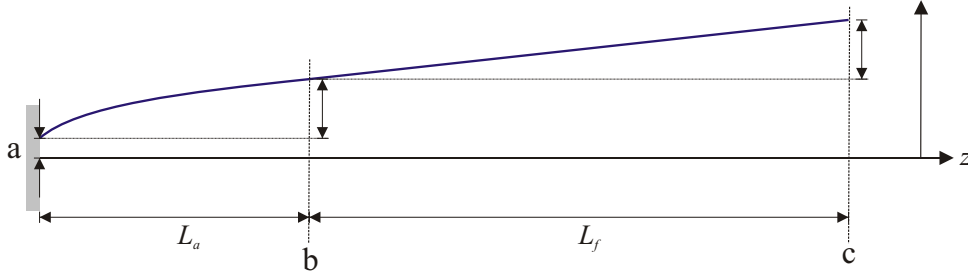


Figure 4.25: Typical trajectory (blue) of an electron in the beam; (a) cathode, (b) anode plane, (c) detector plane. It may start with a small offset ρ_0 from the center axis, it drifts outwards by a length $\Delta\rho_1$ during the acceleration stage, and by another amount $\Delta\rho_2$ during free propagation until it hits the detector.

The particle's final radial coordinate is the sum of three contributions: $\rho = \rho_0 + \Delta\rho_1 + \Delta\rho_2$. The first one may be neglected for the time being². For the second, one has

$$\Delta\rho_1 = v_T \cdot \Delta t_1 \quad \text{with} \quad v_T = \sqrt{\frac{2E_T}{m}} \quad (4.23)$$

²Usually ρ_0 is some tens of microns at most, while ρ is on the order of millimeters.

and Δt_1 can be derived from

$$L_a = \frac{a}{2} \Delta t_1^2 \quad \text{with} \quad a = \frac{eU}{mL_a} \quad (4.24)$$

Combining both equations, one arrives at

$$\Delta \rho_1 = 2L_a \sqrt{\frac{E_T}{E_L}} = 2L_a \frac{v_T}{v_L} \quad (4.25)$$

It is easily verified that the remaining contribution of the free motion is

$$\Delta \rho_2 = L_f \sqrt{\frac{E_T}{E_L}} = L_f \frac{v_T}{v_L} \quad (4.26)$$

Now ρ can be written as

$$\rho = (2L_a + L_f) \frac{v_T}{v_L} = L^* \frac{v_T}{v_L} \quad (4.27)$$

where L^* is the “effective beam line length”. Note that the acceleration in the first section of length L_a is accounted for just by replacing it with a linear motion over the double length $2L_a$, or, equivalently, by inserting half the final longitudinal velocity as a constant velocity of the particle.

Now we have an analytic formula for the transverse velocity distribution of the electrons $f(v_T)$ and a relation between radial position ρ in the beam profile and corresponding v_T . Together, these relations define how the transverse velocity spectrum is mapped to the intensity profile (beam profile) on the detector. For the sake of easier handling and visualization, the term “beam profile” is now always understood as the 1D distribution obtained by integration of the actual 2D beam profile along one axis — only the 1D profiles are compared, since the experiments confirmed that one can assume a cylindrical symmetry of the beam and therefore the full 2D picture does not reveal any additional information relevant here.

The theoretical $f(v_T)$ function was evaluated numerically by a self-written C program (see appendix) that writes a 1D beam profile based on this function into a simple text file, which could be imported by Excel or Origin for plotting. The C program combined the following three steps in one process:

- A virtual quadratic detector screen was assumed, its center coinciding with the beam center where $\rho = 0$. It was rasterized into many pixels, for each pixel (at location (x, y)) the distance to the center ($\rho = \sqrt{x^2 + y^2}$) and the corresponding value of v_T was calculated ($v_T = v_L \cdot \rho/L^*$).
- $f(v_T)$ was calculated for each pixel and for the predetermined energy distribution parameters by integrating (4.22) numerically. Thus, a 2D distribution of electron intensity $f(v_T(x, y))$ was obtained.

- The resulting 2D distribution was integrated along one dimension, completely analogous to the procedure used to plot the 1D beam profiles from the experiment or the simulation, and the 1D profile was written to the text file.

To be more precise, actually the program also tried to imitate the effect of the finite beam emittance, i.e. the fact that the electrons were not emitted at one singular spot, but from a region with a diameter of around 100 microns, where for every location inside this area all emission angles were possible. As a result, the beam is not perfectly laminar, which means that electron trajectories may cross each other, and the assignment of a transverse velocity v_T to a radial position ρ is not really unique. For a given ρ , the value of v_T has an uncertainty defined by the uncertainty in initial radial position ρ_0 of the electron (which was omitted in eq. (4.27)). The numerical algorithm which produced the theoretical beam profiles tried to account for this effect in the following way. For a given radial position ρ on the virtual detector, not only the v_T corresponding to exactly this radius was taken for calculation of $f(v_T)$, but ρ was modified by adding values from $-\rho_0$ to ρ_0 (divided into a few steps) and the corresponding $f(v_T)$ was added in each step. Consequently, the electron count or intensity $I(x, y)$ at a given location specified by (x, y) of a Cartesian coordinate system on the detector screen was not simply $I(x, y) = f(v_T(x, y))$, but

$$I(x, y) = \int_{-\rho_0}^{\rho_0} f(v_T(|\rho + \Delta\rho|)) d\Delta\rho \quad \text{with} \quad \rho = \sqrt{x^2 + y^2} \quad (4.28)$$

Note that normalization did not play any role, since the calculated beam profiles were scaled in the end anyway, setting the maximum of the 1D distribution to one.

Let us now come to the actual purpose of the analytic model. Theoretical beam profiles were fitted to the experimentally observed profiles. To this end, a mathematical model of the velocity distribution $P_v(v)$ had to be assumed, based on an energy spectrum $P_E(E)$. Both distributions are related by

$$P_v(v)dv = P_E(E)dE \quad \text{where} \quad dE = mv dv \quad (4.29)$$

Based on the observations in [23], two alternative energy distribution shapes were used to find the best fit to the experimental data.

1. A truncated Gaussian shape as it was also used in the GPT simulations (see fig. 3.1), to model a rapid drop-off with increasing energy similar to the data shown in fig. 2.8a:

$$P_E(E) \propto e^{-E^2/2\Delta E^2} \quad (4.30)$$

2. An exponential drop-off with increasing energy as it can be seen in fig. 2.8c:

$$P_E(E) \propto e^{-E/\Gamma} \quad \text{with} \quad \Gamma = \Delta E/1.2 \quad (4.31)$$

The energy spread of both shapes is called ΔE and it is defined in such a way that the integral of the respective energy distribution from zero to ΔE contains about 70% of the total number of electrons. For the Gauss shape, it corresponds to the standard deviation, whereas for the exponential shape a conversion factor from Γ to ΔE was found with the ansatz

$$\frac{\int_0^{\Delta E} e^{-E/\Gamma} dE}{\int_0^{\infty} e^{-E/\Gamma} dE} = 1 - e^{-\Delta E/\Gamma} \stackrel{!}{=} 0.7 \quad (4.32)$$

The fitting of theoretical beam profiles to experimental profiles was achieved by trying both models for the spectrum and varying the parameter ΔE .

The experimental beam profiles were all recorded with the grid anode installed, which was large enough to make sure that the electron beam was not clipped at the aperture, as it could happen with the hole anode (see section 4.2.2). Additionally, an increase in beam divergence by the defocusing effect of the electric field near the hole (see section 3.3.3) was avoided. Of course, the beam was affected by the grid and its small-scale field inhomogeneities (forming mesh patterns, see again section 4.2.2), but those patterns got blurred to a large extent when the 2D profiles were integrated down to 1D, their remnants only visible as a more or less strong ripple structure superimposed on the near-Gaussian profiles. As already stated, due to weaker focusing of the 266 nm laser beam, the UV-generated photoelectron beam did usually not show those structures, but for the sake of a fair comparison, CCD shots were also taken from the UV-emitted electron beam with visible grid patterns (achieved by focusing the UV a bit tighter).

Experimental beam profiles and theoretical fits are shown in figures 4.26, 4.27 and 4.28. In each case, four representative experimentally observed beam profiles are superimposed, to give an idea of the typical profile shape and width, and the theoretical curves were fitted to exactly those profiles shown.

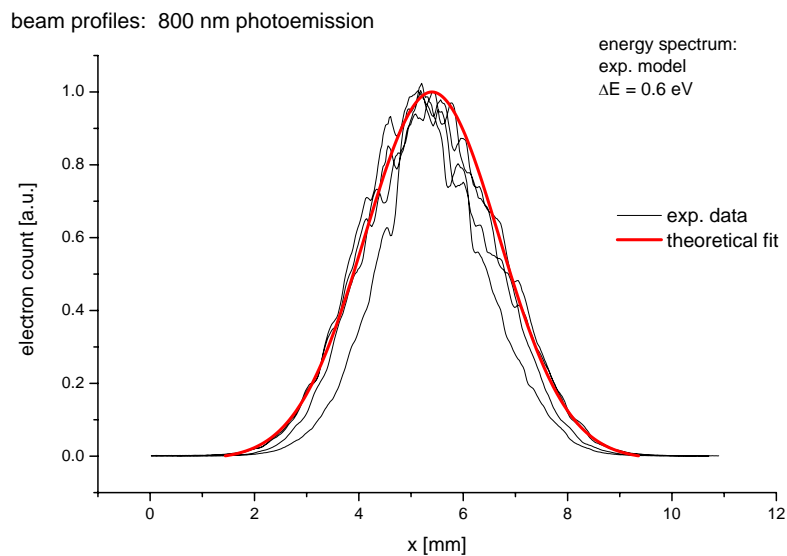


Figure 4.26: Profiles of the electron beam triggered by 800 nm light pulses. The theoretical curve is based on the assumption of an exponential shape of the spectrum with $\Delta E = 0.6 \text{ eV}$.

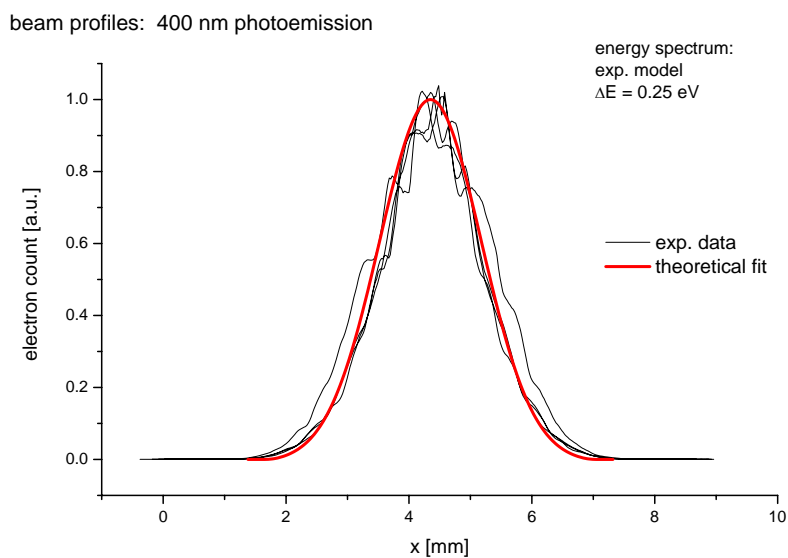


Figure 4.27: Profiles of the electron beam triggered by 400 nm light pulses. The energy distribution used for the fit had an exponential shape with $\Delta E = 0.25 \text{ eV}$.

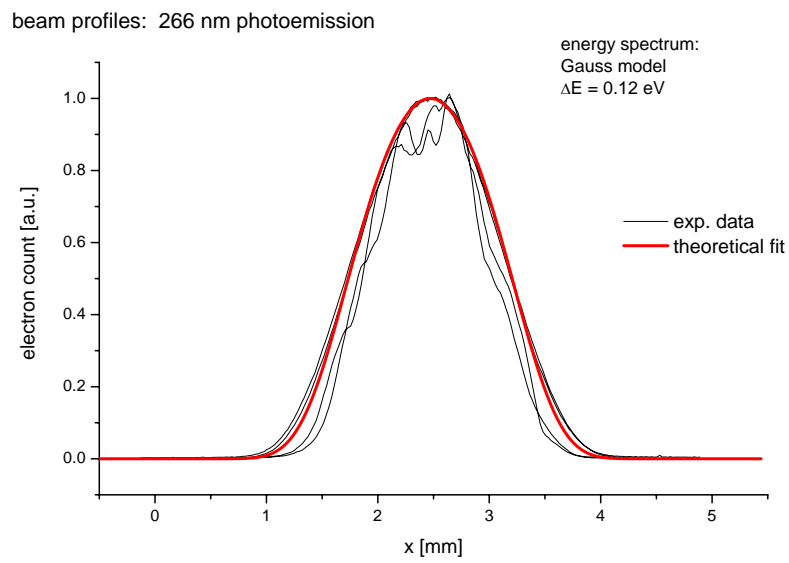


Figure 4.28: Profiles of the electron beam triggered by 266 nm light pulses. Shown are samples with grid pattern in the profile (irregular shape) and without. To have a more conservative fit, the theoretical curve matches the broader profiles rather than the slimmer, which means somewhat higher photoelectron energy spreads. The energy spectrum had a Gauss shape with $\Delta E = 0.12 \text{ eV}$.

The results of the theoretical profile fits are summarized in the following table, where the initial photoelectron energy spread ε_i is identified with the energy spread parameter which was called ΔE .

	shape of electron spectrum	ε_i [eV]
800 nm (multi-photon) photoemission	exponential	0.6
400 nm (two-photon) photoemission	exponential	0.25
266 nm (single-photon) photoemission	truncated Gaussian	0.12

Because of the quite indirect procedure how these values were obtained, they can of course only be understood as an estimation, and there could be an uncertainty of about $\pm 50\%$. Nevertheless, from eq. (4.21) it is clear that the beam profile does contain information about the initial energy spectrum of the electrons. The high uncertainty is not contained in the fitted parameter ΔE (which has an error $\leq 10\%$) but stems from the need to make three additional assumptions, which are listed here again.

1. There is no correlation between energy and velocity direction of an electron.
2. There are no preferred orientations of the electron velocities, i.e. the emission is isotropic into the full half-sphere.
3. A simple model function for the photoelectron energy distribution is chosen, insinuating a specific shape of the spectrum.

No literature was found providing satisfactory information regarding those details of photoemission processes. However, the theory based on those presumptions was in good accordance with experimental data. For matching calculated and measured beam profiles, only one free parameter, the energy spread, had to be varied.

Chapter 5

Conclusion

In this diploma thesis, an electron gun was built and characterized which is intended to be further developed into a source of ultrashort electron pulses. It was driven by a special femtosecond oscillator, and it produced, for the first time, electron pulses with MHz repetition rate. The number of electrons per pulse could be kept on the order of one in a controlled and reproducible way in order to minimize space-charge effects, which was one of the central goals of the project. Computer simulations were made to estimate the electron pulse lengths that can be expected from the proposed bunching scheme, revealing that a minimum pulse duration of a few femtoseconds should be possible. In these simulations it was found that electron bunches may get deformed by the anode structure in such a way that the pulse length in the temporal focus is increased. This discovery triggered more detailed studies on this problem, see [19].

The experimental work was focused on finding the most suitable photoemission process to produce an electron beam with enough intensity, a clean profile and a low energy spread in a reproducible way. Two different cathode materials (gold, copper) and different layer thicknesses were compared. The results indicate that gold is the more suitable material, and that one could possibly achieve the same electron yield with less laser power if the layer thickness is reduced, e.g. to about 20 nm instead of 50 nm. In addition, photoemission with different photon energies (the laser fundamental and its second and third harmonic) was examined. It was found that

- photoemission with 800 nm light was a high-order process (probably involving above-threshold photoemission), it required a considerable fraction of the oscillator's energy output, was not well reproducible in terms of electron yield and beam profile, and it imposed the largest energy spread on the electrons.
- photoemission with 400 nm (second harmonic) light was a second-order process (requiring two photons to emit one electron) which is so much more efficient that laser pulse energies of around 1% of the full pulse energy are adequate for the same beam focusing. Reproducibility was much better, the electron beam profile was very clean and nearly Gaussian, and the particles' initial energy spread was lower, around 0.3 eV.

- UV light with 266 nm wavelength (third harmonic) and hence a photon energy of 4.65 eV made a one-photon (first-order) photoemission possible, requiring only a fraction on the order of 10^{-4} to 10^{-3} of the available laser power. Extremely smooth electron beam profiles were obtained, and the initial energy spread of the emitted electrons clearly was by far the lowest, ranging around 0.1 eV.

For the generation of the third harmonic, two alternative mechanisms were tried. The first was surface-enhanced THG, which was found to be possible, but too inefficient. Besides, it was not very practical because of frequent damaging of the necessary surface layer. Instead, the cascaded scheme of SHG and subsequent SFG was used, which showed enough conversion efficiency. Regarding the electron beam properties, usage of the third harmonic is clearly the best option for driving the electron gun, but its drawback is the fluctuation of the UV power caused by variations of the spectral width of the oscillator output.

A method was developed which allows, under certain assumptions, the theoretical reconstruction of the initial energy spread of the photoelectrons based on the electron beam profile. A C program was written to calculate theoretical beam profiles numerically, and these profiles were fitted to those observed experimentally by varying the energy spread as a parameter. A value of such a spread was found for all three kinds of photoemission. The most important result is the qualitative conclusion that the UV laser pulses deliver electron pulses with an energy spread significantly lower than the visible light does.

Measuring the length of an ultrashort electron pulse is far from trivial and was not part of this work, so there is no experimental evidence of how short the pulses were without the bunching. Nevertheless, in fig. 3.3, on p. 25, simulation data is presented which indicates, for an initial energy spread of 0.1 eV, a second-moment pulse duration around 300 fs.

The observations made in this thesis and the possibility to create electron pulses at MHz repetition rate which do not suffer broadening due to space-charge pave the way towards the planned RF bunching to attain sub-10 fs electron pulses for UED experiments.

Appendix

```
// beamprofile.cpp

#include <stdio.h>
#include <math.h>

#define ECHARGE      1.602e-19 //C
#define EMASS        9.109e-31 //kg
#define PI          3.141592654

#define NSTEPS      100

#define SHAPE_GAUSS    1
#define SHAPE_EXP      2

double deltaE;
double sigma_energy;
double sigmasquared;
double gamma_energy;
double vmax;
double xmax;
double delta_r0;

short spectralshape;

double spectrum( double v )
{
    double energy;

    energy = 0.5*EMASS*v*v;
```

```

if( spectralshape == SHAPE_GAUSS )
{
    // Gaussian around center energy
    return v * exp( -energy*energy/(2*sigmasquared) );
}
else if( spectralshape == SHAPE_EXP )
{
    // exponential (Maxwell-like)
    return v * exp( -energy/gamma_energy );
}
else
    return 0;
}

double P_of_vt( double vt )
{
    double P = 0;
    double v, dv;
    double angularfactor, spectrumfactor;
    double energy, theta, costheta;

    if( vt < 0 || vt >= vmax )
        return 0.0;
    if( vmax <= 0 )
        return 0.0;

    // integration over v
    dv = vmax / 3000.0;
    v = vt + dv; // to avoid singularity at v=vt, set the lower integration boundar
    while( v <= vmax )
    {
        theta = asin(vt/v);
        costheta = cos(theta);
        angularfactor = 1.0 / ( v * costheta );
        spectrumfactor = spectrum( v );

        P = P + ( angularfactor * spectrumfactor ) * dv;

        v = v + dv;
    }

    return P;
}

```

```

double I_of_x( double x )
{
    double rmax = xmax;
    double r, y, dy, vt, I;
    double factor = 8.1e7/0.354;
    double P = 0;
    short i = 0;
    double r_modified;

    // mimic the integration of a 2D profile down to 1D
    I = 0.0;
    dy = rmax / 100.;
    for( y = 0; y <= rmax; y = y + dy )
    {
        r = sqrt( x*x + y*y );
        if( r > rmax )
            continue;

        P = 0;
        for( i = -2; i <= 2; i++ )
        {
            r_modified = r + (double)i*0.5*delta_r0;
            vt = abs( factor * r_modified );
            P = P + P_of_vt( vt );
        }

        I = I + P/5.0 * dy;
    }

    return 2.0*I;
}

```

```

int main(int argc, char* argv[])
{
    double x, I;
    FILE* file;
    double Idist[NSTEPS];
    double Ipeak = 0.0;

    spectralshape = SHAPE_EXP;
}

```

```

deltaE = 0.6*ECHARGE; // J
if( spectralshape == SHAPE_GAUSS )
{
    sigma_energy = deltaE;
    sigmasquared = sigma_energy*sigma_energy;
}
else if( spectralshape == SHAPE_EXP )
{
    gamma_energy = deltaE / 1.2;
}
vmax = sqrt(2.0*(4.0*deltaE)/EMASS); // m/s
xmax = 4e-3; // m
delta_r0 = 0.1e-3; // m

// calculate profile
for( short i = 0; i < NSTEPS; i++ )
{
    x = xmax/(double)NSTEPS * (double)i;

    I = I_of_x( x );

    Idist[i] = I;
    if( Ipeak < I )
        Ipeak = I;

    printf( "%i percent done\n", i*100/NSTEPS );
}

// write data to file
file = fopen( "profile.txt", "w" );
for( short i = -NSTEPS+1; i < NSTEPS; i++ )
{
    x = xmax/(double)NSTEPS * (double)i;

    I = Idist[abs(i)];
    if( Ipeak > 0 ) I = I / Ipeak;

    fprintf( file, "%e %e \n", x, I );
}
fclose( file );

return 0;
}

```

Bibliography

- [1] T. Brabec and F. Krausz, “Intense few-cycle laser fields: Frontiers of nonlinear optics”, *Rev. Mod. Phys.*, **72** (2000), 545–591
- [2] L. Schäfer, “Electron Diffraction as a Tool of Structural Chemistry”, *Appl. Spectrosc.*, **30** (1976), 123
- [3] R. Srinivasan, V.A. Lobastov, C. Ruan and A. H. Zewail, “Ultrafast Electron Diffraction”, *Helv. Chim. Acta*, **86** (2003), 1763
- [4] A. H. Zewail, “4D Ultrafast Electron Diffraction, Crystallography, and Microscopy”, *Ann. Rev. Phys. Chemistry*, **57** (2006), 65
- [5] S. Naumov, A. Fernandez, R. Graf, P. Dombi, F. Krausz and A. Apolonski, “Approaching the microjoule frontier with femtosecond laser oscillators”, *New Journal of Physics*, **7** (2005), 216
- [6] E. Fill, L. Veisz, A. Apolonski and F. Krausz, “Sub-fs electron pulses for ultrafast electron diffraction”, *New Journal of Physics*, **8** (2006), 272
- [7] M. Monastyrskiy, S. Andreev, V. Tarasov and M. Schelev, *Proc. of SPIE* Vol. 4948, SPIE (2003), 305–310
- [8] S. Andreev, D. Greenfield, M. Monastyrskiy, V. Tarasov and M. Schelev, *Proc. of SPIE* Vol. 5398, SPIE (2004), 1–15
- [9] J. R. Helliwell, P. M. Rentzepis (eds.), *Time-resolved Diffraction*, Clarendon Press (Oxford, 1997)
- [10] B. J. Siwick, J. R. Dwyer, R. E. Jordan and R. J. Dwayne Miller, “An atomic-level view of melting using femtosecond electron diffraction”, *Science*, **302** (2003), 1382
- [11] R. C. Dudek and P. M. Weber, “Ultrafast Diffraction Imaging of the Electrocyclic Ring-Opening Reaction of 1,3-Cyclohexadiene”, *J. Phys. Chem.*, **105** (2001), 4167
- [12] J. C. Williamson and A. H. Zewail, “Ultrafast electron diffraction. Velocity mismatch and temporal resolution in crossed-beam experiments”, *Chem. Phys. Lett.*, **209** (1993), 10
- [13] P. Baum and A. H. Zewail, “Breaking resolution limits in ultrafast electron diffraction and microscopy”, *PNAS*, **103** (2006), 16105–16110

- [14] N. Naumova, I. Sokolov, J. Nees, A. Maksimchuk, V. Yanovsky, and G. Mourou, “Attosecond electron bunches”, *Phys. Rev. Lett.*, **93** (2004), 195003
- [15] S. E. Irvine and A. Y. Elezzabi, “Femtosecond electron pulse gating using surface plasmons”, *Optics Express*, **14** (2006), 4115–4127
- [16] J. B. Hastings, F. M. Rudakov, D. H. Dowell, J. F. Schmerge, J. D. Cardoza, J. M. Castro, S. M. Gierman, H. Loos and P. M. Weber, “Ultrafast time-resolved electron diffraction with megavolt electron beams”, *Appl. Phys. Lett.*, **89** (2006), 184109
- [17] V. A. Lobastov, R. Srinivasan and A. H. Zewail, “Four-dimensional ultrafast electron microscopy”, *PNAS*, **102** (2005), 7069–7073
- [18] M. Monastyrskiy, S. Andreev, D. Greenfield, G. Bryukhnevich, V. Tarasov and M. Schelev, “Computer modeling of a subfemtosecond photoelectron gun with time-dependent electric field for TRED experiments”, *Proc. of SPIE* Vol. 5580, SPIE (2005), 324–333
- [19] L. Veisz, G. Kurkin, K. Chernov, V. Tarnetsky, A. Apolonski, F. Krausz and E. Fill, “Hybrid dc-ac electron gun for fs-electron pulse generation”, *New Journal of Physics*, **9** (2007), 451
- [20] E. Wilson, *An Introduction to Particle Accelerators*, Oxford Univ. Press (Oxford, 2001), 147–150
- [21] E. Fill, L. Veisz, A. Apolonski and F. Krausz, “Femtosecond electron gun for diffraction experiments”, *Proc. of SPIE*, Vol. 6194 (SPIE, 2006), 61940J
- [22] L.-S. Ma, R. K. Shelton, H. C. Kapteyn, M. M. Murnane and J. Ye, “Sub-10-femtosecond active synchronization of two passively mode-locked Ti:sapphire oscillators”, *Phys. Rev. A*, **64** (2001), 021802
- [23] M. Aeschlimann, C. A. Schmuttenmaer, H. E. Elsayed-Ali, R. J. D. Miller, J. Cao, Y. Gao and D. A. Mantell, “Observation of surface enhanced multiphoton photoemission from metal surfaces in the short pulse limit”, *J. Chem. Phys.*, **102** (1995), 8606
- [24] T. Tsang, T. Srinivasan-Rao and J. Fischer, “Surface-plasmon field-enhanced multiphoton photoelectric emission from metal films”, *Phys. Rev. B*, **43** (1991), 8870
- [25] Official website: <http://www.pulsar.nl/gpt/>
- [26] V. L. Kalashnikov, E. Podivilov, A. Chernykh, S. Naumov, A. Fernandez, R. Graf and A. Apolonski, “Approaching the microjoule frontier with femtosecond laser oscillators: theory and comparison with experiment”, *New Journal of Physics*, **7** (2005), 217
- [27] W. R. Trutna and R. L. Byer, “Multiple-pass Raman gain cell”, *Appl. Optics*, **19** (1980), 301

- [28] A. Sennaroglu, A. M. Kowalevich, Jr., E. P. Ippen and J. G. Fujimoto, “Compact Femtosecond Lasers Based on Novel Multipass Cavities” *IEEE Journal of Quantum Electronics*, **40** (2004), 519
- [29] J. Alda, “Laser and Gaussian Beam Propagation and Transformation”, in: R. G. Driggers (ed.), *Encyclopedia of Optical Engineering*, Marcel Dekker Ltd. (New York, 2003)
- [30] R. W. Boyd, *Nonlinear Optics* (2nd ed.), Academic Press (San Diego / London, 2003), 94–99
- [31] G. P. Agrawal, R. W. Boyd (eds.), *Contemporary Nonlinear Optics*, Academic Press (San Diego, 1992), 134–140
- [32] F. Krausz, *Photonics I – The theory of light and its advanced applications*, lecture notes (2006), available online at:
<http://www.attoworld.de/education/lecturecourses.html>
- [33] J.-C. Diels, W. Rudolph, *Ultrashort Laser Pulse Phenomena* (2nd ed.), Academic Press (San Diego, 2006), 175
- [34] A. E. Siegman, *Lasers*, University Science Books (Sausalito, 1986)
- [35] D. Stoker, M. F. Becker and J. W. Keto, “Optical third-harmonic generation using ultrashort laser pulses”, *Phys. Rev A*, **71** (2005), 061802
- [36] P. Dombi, A. Apolonski, Ch. Lemell, G. G. Paulus, M. Kakehata, R. Holzwarth, Th. Udem, K. Torizuka, J. Burgdörfer, T. W. Hänsch and F. Krausz, “Direct measurement and analysis of the carrier-envelope phase in light pulses approaching the single-cycle regime”, *New Journal of Physics*, **6** (2004), 39
- [37] H. B. Michaelson, “The work function of the elements and its periodicity”, *J. Appl. Phys.*, **48** (1977), 4729
- [38] D. R. Lide, *Handbook of Chemistry and Physics*, 85th ed. 2004–2005, CRC Press (Boca Raton, 2004), 12-136
- [39] W. G. Driscoll (ed.) and W. Vaughan (assoc. ed.), *Handbook of Optics*, McGraw-Hill (New York, 1978), 10-4

Acknowledgements

First of all, I want to thank Prof. Ferenc Krausz (MPQ¹, LMU²), for giving me the opportunity to work in his highly renowned research group, and Prof. Alfred Laubereau from the TUM³ for taking over the official mentoring of this work from the side of my alma mater.

I especially would like to thank both my supervisors: Dr. Alexander Apolonskiy (LMU) for believing in me and his support, and Dr. Ernst Fill (MPQ) for his strong interest in my work, his readiness to help or discuss problems whenever needed, and of course for supplying me with all kinds of material.

Furthermore I would like to thank Roswitha Graf (LMU) for her great and immediate help in the lab whenever needed, especially in all respects concerning the laser system used and for setting up the laser pulse compressor, and Dr. Sergei Naumov (former group member) for his help in this field in the beginning of my work.

I want to thank Peter Reckenthäler (MPQ) for his personal support, his help in the lab and for giving me valuable advice, as well as Dr. Martin Centurion (MPQ) for his help and fruitful ideas. Thanks to Dr. Laszlo Veisz for helping me in some questions regarding GPT simulations and surface THG.

I would like to thank Dagmar Frischke (LMU) who was so kind to help me by fabricating the thin metal films for the cathodes although she is not part of the research group, and Dr. Volodymyr Pervak for providing me with all necessary mirrors and special optical coatings. Of course, also many thanks to the whole rest of the LMU group for help and the friendly working atmosphere, particularly to Marion Kraus for her supporting work.

Last but not least, I want to thank my parents for encouraging me and making my studies of physics possible in the first place, my friends for motivation and distraction when needed, and my whole family and my girlfriend for their love and support!

Daniel Wytrykus

¹Max-Planck-Institute of Quantum Optics

²Ludwig-Maximilians-Universität München

³Technische Universität München